JGR Oceans

RESEARCH ARTICLE
10.1029/2024JC021814

Key Points:

- Drifting buoys deployed in Hurricane Idalia (2023) are combined with model winds to study waves in a storm-following reference frame
- Spectral mean square slopes are elevated in the right-rear quadrant of the storm where wind and waves are aligned
- Wind-wave alignment is predictive of deviations in mean square slope from a primary wind speed dependence

Correspondence to:
J. R. Davis,
davisjr@uw.edu

Citation:
Davis, J. R., Thomson, J., Houghton, I. A., Fairall, C. W., Butterworth, B. J., Thompson, E. J., et al. (2025). Ocean surface wave slopes and wind-wave alignment observed in Hurricane Idalia. *Journal of Geophysical Research: Oceans*, *130*, e2024JC021814. https://doi.org/10.1029/2024JC021814

Received 6 SEP 2024
Accepted 31 JAN 2025

Author Contributions:
Conceptualization: Jacob R. Davis, Jim Thomson, Isabel A. Houghton, Chris W. Fairall
Data curation: Jacob R. Davis, Isabel A. Houghton
Formal analysis: Jacob R. Davis
Funding acquisition: Jim Thomson, Isabel A. Houghton, Chris W. Fairall, Elizabeth J. Thompson, Gijs de Boer, James D. Doyle, Jonathan R. Moskaitis
Investigation: Jacob R. Davis, Jim Thomson, Isabel A. Houghton, Brian J. Butterworth
Methodology: Jacob R. Davis, Jim Thomson, Isabel A. Houghton, Gijs de Boer, James D. Doyle, Jonathan R. Moskaitis
Project administration: Jim Thomson, Isabel A. Houghton, Chris W. Fairall, Elizabeth J. Thompson, Gijs de Boer, James D. Doyle, Jonathan R. Moskaitis

Ocean Surface Wave Slopes and Wind-Wave Alignment Observed in Hurricane Idalia

Jacob R. Davis[1], Jim Thomson[1], Isabel A. Houghton[2], Chris W. Fairall[3], Brian J. Butterworth[3,4], Elizabeth J. Thompson[3], Gijs de Boer[3,4], James D. Doyle[5], and Jonathan R. Moskaitis[5]

[1]Applied Physics Laboratory, University of Washington, Seattle, WA, USA, [2]Sofar Ocean, San Francisco, CA, USA, [3]NOAA Physical Sciences Laboratory (PSL), Boulder, CO, USA, [4]Cooperative Institute for Research in Environmental Sciences (CIRES), University of Colorado Boulder, Boulder, CO, USA, [5]U.S. Naval Research Laboratory, Monterey, CA, USA

Abstract Drifting buoy observations in Hurricane Idalia (2023) are used to investigate the dependence of ocean surface wave mean square slope on wind, wave, and storm characteristics. Mean square slope has a primary dependence on wind speed that is linear at low-to-moderate wind speeds and approaches saturation at high wind speeds (>20 m s^{-1}). Inside Hurricane Idalia, buoy-measured mean square slopes have a secondary dependence on wind-wave alignment: at a given wind speed, slopes are higher where wind and waves are aligned compared to where wind and waves are crossing. At moderate wind speeds, differences in mean square slope between aligned and crossing conditions can vary 15%–20% relative to their mean. These changes in wave slopes may be related to the reported dependence of air-sea drag coefficients on wind-wave alignment.

Plain Language Summary Wave slope, or the ratio of a wave's height to its length, is explored in connection to wind and wave characteristics within Hurricane Idalia (2023). Slopes primarily depend on wind speed: waves steepen quickly in low-to-moderate wind conditions, but this rate of increase drops drastically at the high wind speeds found in hurricanes. At a given wind speed, buoy data from Hurricane Idalia reveal a dependence of slope on the relative alignment of the wind and wave directions. Slopes are elevated when the wind blows in the same direction the waves travel and are reduced when the wind blows roughly perpendicular to the waves. Wave slope, particularly of the shorter waves, is related to the roughness of the ocean surface, which is critical to modeling wind surface forcing (or "drag") in hurricanes. Understanding variations in slope within hurricanes thus helps to inform the prediction models used for hurricane intensity and coastal flooding forecasts.

1. Introduction

Hurricane-generated ocean surface waves drive the exchange of heat and momentum at the air-sea interface and also contribute to coastal flooding and erosion. A major mechanism by which waves influence these processes is through the modulation of air-sea drag. Although wind stress generally increases with wind speed, the rate at which it increases, often described by an air-sea drag coefficient, is complex and under continued investigation. Growing evidence suggests the air-sea drag coefficient depends on sea state through wave age (Drennan et al., 2003; Edson et al., 2013; Janssen, 1989; Toba et al., 1990), wave slope (Edson et al., 2013; Taylor & Yelland, 2001), and more recently, wind-wave alignment (Holthuijsen et al., 2012; Zhou et al., 2022; Potter et al., 2022; S. Chen et al., 2022; Husain et al., 2022; Manzella et al., 2024). This is critical in hurricanes, since the drag coefficient parameterization used in forecast models influences the simulated intensity of a hurricane (C. Davis et al., 2008; Emanuel, 2003).

Inside a hurricane, waves are complex and spatially varying. Characteristics such as wave height and direction are asymmetric with respect to the center, and wave growth depends on the size, strength, and translational speed of a storm (Young, 2003). The largest waves are typically found on the right side of the hurricane with respect to the direction of translation (in the Northern Hemisphere), where the storm and the winds are moving in the same direction as the waves while they are being generated (Collins et al., 2018; Hu & Chen, 2011; Tamizi & Young, 2020; C. W. Wright et al., 2001). On the right side of the storm, general alignment of the hurricane's motion and winds results in an "extended" (or "moving") fetch, whereby the waves traveling in the same direction as the storm remain in the wind for an extended period of time (King & Shemdin, 1978).

Resources: Jacob R. Davis, Jim Thomson, Isabel A. Houghton, Chris W. Fairall, Elizabeth J. Thompson, Gijs de Boer, James D. Doyle, Jonathan R. Moskaitis
Software: Jacob R. Davis
Supervision: Jim Thomson, Isabel A. Houghton, Chris W. Fairall, Elizabeth J. Thompson, Gijs de Boer
Validation: Jacob R. Davis
Visualization: Jacob R. Davis, Brian J. Butterworth
Writing – original draft: Jacob R. Davis, Jim Thomson
Writing – review & editing: Jacob R. Davis, Jim Thomson, Isabel A. Houghton, Chris W. Fairall, Brian J. Butterworth, Elizabeth J. Thompson, Gijs de Boer, James D. Doyle, Jonathan R. Moskaitis

Swell generally propagates outward from the storm center in an "arc" spanning the right-front, left-front, and left-rear quadrants (King & Shemdin, 1978). The alignment of wind and long period waves (which eventually become swell) within hurricanes, or *wind-wave alignment*, is the subject of some of the earliest research on hurricane waves (Arakawa, 1954; Tannehill, 1936). Misalignment is typically observed on the left half of the storm, and it is often reported to be greater in the left-rear quadrant (Black et al., 2007; Hu & Chen, 2011; Schönau et al., 2024; Tamizi & Young, 2020; Tannehill, 1936). Outward wave propagation in the front of the storm frequently causes slight misalignment to occur in the right-front quadrant (Hu & Chen, 2011; King & Shemdin, 1978). Most studies report the closest wind-wave alignment in the right-rear quadrant, with some suggesting this is due to the sea state in this quadrant being mostly comprised of locally generated waves, and not previously generated swell which has propagated from another region of the storm (Arakawa, 1954; Collins et al., 2018; Hu & Chen, 2011; Hwang et al., 2017; Tamizi & Young, 2020; Young, 2006). Notable exceptions exist, with some observations showing alignment to the right-front of the storm and crossing, disorganized wind-waves to the right-rear (Holthuijsen et al., 2012; Schönau et al., 2024). The alignment of mean wind direction and dominant wave direction has been shown to have a sinusoidal dependence on azimuth (Hwang et al., 2017; Kudryavtsev et al., 2021).

One dimensional (i.e., scalar wave energy) frequency spectra inside hurricanes are typically unimodal, but can be bimodal (or even trimodal), particularly on the left side where wind-sea and longer period waves propagate in different directions (J. D. Doyle, 2002; Young, 2006; Hu & Chen, 2011; Hwang et al., 2017; Tamizi & Young, 2020; Hsu, 2021). The high frequency tail of observed hurricane spectra span the range of canonical shapes: in a typical spectrum, the energy just beyond the spectral peak is expected to decay as the frequency power-law f^{-4} characteristic of the equilibrium range (wind input balanced by dissipation from breaking and nonlinear energy fluxes) (Phillips, 1985; Toba, 1973). Beyond this range, the spectrum transitions to an f^{-5} saturation range (wind input is balanced by dissipation from breaking) until frequencies approach those of gravity-capillary and capillary waves (Banner, 1990; Forristall, 1981; Lenain & Melville, 2017; Romero et al., 2012). Tamizi and Young (2020) fit their hurricane wave observations from buoys to a generalized Joint North Sea Wave Project (JONSWAP) spectral model and find the spectral tail steepens from f^{-4} to f^{-5} with decreasing wave age, where wave age is the ratio of wave phase speed to wind speed. The mean of their slope exponent observations is -4.68. Drifting buoy observations suggest the tail becomes dominated by the f^{-5} saturation range above wind speeds of 25 m s^{-1} at frequencies spanning from the peak frequency to the maximum resolved frequency of 0.5 Hz (J. Davis et al., 2023). Hwang et al. (2017) find substantial scatter in their observed spectral slopes (between -4 and -5), and instead suggest the treatment of the spectral slope exponent as a random variable. The Gaussian fit to their data has a mean of -4.48 and standard deviation of 0.53.

Mean square slope (mss) is an integral quantity closely related to the shape and total energy of the spectral tail. It is frequently used as an integral metric for model spectral comparisons (Elfouhaily et al., 1997; Reichl et al., 2014; Romero & Lubana, 2022). When calculated from the wave spectrum, mss is the second moment in the wavenumber domain:

$$\text{mss} = \int_{k_1}^{k_2} k^2 E(k)dk \tag{1}$$

where $E(k)$ is elevation variance spectral density as a function of wavenumber, k, which is integrated over limits k_1 and k_2. With energy proportional to wave amplitude, a, squared, as $E(k) \sim a^2$, Equation 1 yields an expression proportional to wave slope characterized by the product of amplitude and wavenumber squared, $(ak)^2$. Buoys (and other point measurements) measure energy in the frequency domain, $E(f)$, thus mss estimates rely on the dispersion relationship to relate frequency to wavenumber:

$$(2\pi f)^2 = gk\tanh(kh) \tag{2}$$

where g is the acceleration of gravity and h is water depth. The quantity kh is the relative depth, which determines the effect of depth on wave properties. Equation 2 can be used in all water depths and is valid in the reference frame intrinsic to the waves (see Section 2.4). Energy spectra also need to be transformed from the frequency domain to the wavenumber domain using

$$E(k) = E(f)\frac{df}{dk} \tag{3}$$

where $df/dk = c_g/(2\pi)$ is a Jacobian proportional to group velocity, c_g, calculated using wavenumber and depth (Holthuijsen, 2007). An explicit expression for mss can also be derived by substituting the deep water limit of the dispersion relation, $k = (2\pi f)^2/g$, into Equation 1. The k^2 dependence of Equation 1 yields an f^4 dependence in the frequency domain.

The magnitude of mss is sensitive to the wavelength (or frequency) extent, thus the magnitude varies widely across instruments. Optical methods, such as the sun glint measurements of Cox and Munk (1954), lidar (Lenain et al., 2019), or polarimetry (Zappa et al., 2008), approach estimates of the "total" mean square slope (despite broad wavelength coverage, the long and short wavelength limits of mss estimates from these methods are constrained by field of view and pixel resolution, respectively). A total mean square slope is equivalent to Equation 1 integrated from $k_1 \simeq 0$ rad m^{-1} to $k_2 \simeq \infty$.

Other methods that resolve mss over a shorter range of wavelengths, such as buoys (J. Davis et al., 2023) and radar (Gleason et al., 2018), have smaller mss. The k^2 dependence of Equation 1 weights the tail of the spectrum which contains the high frequency, short wavelength waves. At low-to-moderate wind speeds and wave conditions, a substantial portion of the total mean square slope magnitude is contributed by short waves typically not measurable by buoy and radar (Lenain & Melville, 2017).

Mean square slope (mss) has a primary dependence on wind speed. Most observations suggest mss, resolved down to wavelengths ranging from several meters to less than a centimeter, has an approximately linear relationship to wind speed up to 15–20 m s^{-1} (Bréon & Henriot, 2006; Cox & Munk, 1954; J. Davis, Thomson, Butterworth, et al., 2024; Guérin et al., 2022; Jackson et al., 1992; Lenain et al., 2019;). Other observations have found logarithmic (Ross & Dion, 2007; Vandemark et al., 2004; Walsh et al., 1998; Wu, 1990) or power-law (Hauser et al., 2008; P. Chen et al., 2018) relationships over similar wavelengths and wind speeds.

In hurricanes, mss approaches quasi-saturation at high wind speeds as measured by buoys (J. Davis et al., 2023; Shimura et al., 2024) and radar (J. Davis, Thomson, Butterworth, et al., 2024; Gleason et al., 2018; Hwang et al., 2021; Katzberg et al., 2013). L-band GPS reflectometry measurements in hurricanes (0.57 m minimum wavelength) have a logarithmic dependence on wind speed and increase a little with growing wind speed beyond 25 m s^{-1} (Hwang et al., 2021). Buoy-based mss estimates (6 m minimum wavelength) measured in hurricanes effectively saturate beyond 25 m s^{-1} and can be described using a tanh relationship up to 54 m s^{-1} (J. Davis et al., 2023). Mean square slopes estimated by the Wide Swath Radar Altimeter (WSRA), a Ku-band radar which flies aboard the "Hurricane Hunter" P-3s (0.2 m minimum wavelength), are linear up to 20 m s^{-1}, saturate around 25 m s^{-1}, and even reduce slightly at higher wind speeds (J. Davis, Thomson, Butterworth, et al., 2024; Pop-Stefanija et al., 2021; Walsh et al., 2014).

Mean square slope has been shown to have a secondary dependence (variation at a given wind speed) on atmospheric stability. Hwang and Shemdin (1988) find slopes are lower in stable conditions, which was also supported by subsequent laser glint measurements (Shaw & Churnside, 1997). Lenain et al. (2019) were unable to find an mss dependence on atmospheric stability using the Richardson number, though their observations mostly consisted of neutral to unstable conditions. Other works have reported a dependence on fetch (Donelan, 2018; Vandemark et al., 2004); however the modeled mss of Donelan (2018) suggest this dependence is weak until wind speeds exceed 30 m s^{-1}, beyond which the influence of fetch varies. Vandemark et al. (2004) find mss of waves longer than 2-m measured near the coast to be smaller than in the open ocean, which Sun et al. (2001) had previously attributed to energy transfer from short to long waves via wave-wave interaction. Close to shore (within 2 km), mss first increases due to shoaling and then decreases drastically due to active breaking in the surf zone (Anctil & Donelan, 1996; Sun et al., 2001). In hurricanes, Hwang and Fan (2018) report that their parametric model of mss (based on observations) has a secondary dependence on wind field asymmetry, varying 10%–15% at a given wind speed and generally increasing as asymmetry grows. Their mss has a weak secondary dependence on the radius of maximum wind.

The spectral tail, which can be characterized by mss, is closely tied to wind forcing. Within the f^{-4} equilibrium range, the wind friction velocity is proportional to mss (Phillips, 1985; Plant, 1982). Wave-derived wind stress estimates compare well to direct covariance flux observations in wind speeds from 5 m s^{-1} to 15 m s^{-1} (Thomson et al., 2013). Energy levels in the equilibrium range can be used to derive proxy wind speeds from measurements of the wave spectrum (Mudd et al., 2024; Shimura et al., 2022; Voermans et al., 2020). The empirical relationship between mss and wind speed is frequently used to infer wind speed using satellite mss observations (Clarizia & Ruf, 2016; Gleason et al., 2018; Hauser et al., 2017) as well as surface buoy mss observations (Zhong et al., 2022).

When resolved down to sufficiently small wavelengths, mss is widely interpreted as a measure of roughness (Boisot et al., 2015; Cox & Munk, 1954; Hwang, 2005; Li et al., 2022; Walsh et al., 1998). The air-sea drag coefficient, which sets the rate of momentum transfer between the atmosphere and ocean, is often expressed as a function of a roughness length (Charnock, 1955; Edson et al., 2013). Root mean square slope, $\sqrt{\mathrm{mss}}$, has previously been used to develop a roughness length parameterization at moderate conditions in the coastal waters of Lake Ontario (Anctil & Donelan, 1996). A similar form was adopted by Taylor and Yelland (2001) in their widely used roughness length parameterization, but with $\sqrt{\mathrm{mss}}$ replaced by a bulk slope calculated as the ratio of significant wave height to peak wavelength. Mean square slope also correlates with wave form drag (Sullivan et al., 2018). Theoretical formulations for form drag depend on the shape and energy levels within the spectral tail, both of which are captured by changes in mss (Donelan et al., 2012; Reichl et al., 2014). At high wind speeds, form drag is the dominant contributor to total drag (Donelan, 2018; Donelan et al., 2012; Sullivan et al., 2018).

At the high wind speeds found in hurricanes, many observational drag coefficient estimates begin to saturate around 25 m s^{-1} to 35 m s^{-1} (Black et al., 2007; Donelan, 2004; Holthuijsen et al., 2012; Powell et al., 2003; Takagaki et al., 2012) (The measurements originally presented in Donelan (2004) have since been revised in Curcic and Haus (2020)). The saturation of drag coefficient with wind speed is qualitatively similar to the dependence of mss on wind speed, which is generally monotonic but increases little beyond 25 m s^{-1} (J. Davis et al., 2023). The observations of Powell et al. (2003) and Holthuijsen et al. (2012) suggest drag coefficient reduces at high wind speeds (>35 m s^{-1}); however more recent studies have raised concerns about substantial uncertainty and bias inherent to the dropsonde profile methods used to estimate surface stress in these prior works (Richter et al., 2016, 2021).

Recent work has demonstrated a dependence of drag coefficient on wind-wave alignment inside hurricanes. Holthuijsen et al. (2012) find drag coefficient, estimated from GPS dropsonde hurricane wind profiles, is reduced when wind and long-period wave directions are crossing below wind speeds of 25 m s^{-1}, but is significantly enhanced from 30 m s^{-1} to 50 m s^{-1} (relative to aligned and opposing wind and waves). Zhou et al. (2022) estimate drag coefficients in hurricanes using a combination of upper-ocean current observations and a coupled ocean-wave model. They report a significant reduction in drag coefficient above 25 m s^{-1} when wind-wave alignment exceeds 45°. Large Eddy Simulations of monochromatic waves, with a wave age characteristic of tropical cyclones, suggest drag coefficient is reduced when wind-wave alignment exceeds 22.5–45° (Manzella et al., 2024).

Here, we use wave observations from a densely populated array of drifting buoys in Hurricane Idalia (2023) to explore the secondary dependencies of mss within hurricanes. Based on the connection of mss to the spectral tail, we hypothesize mss will have a secondary dependence on wind-wave alignment in hurricanes that is similar to that of drag. Although a related data set of observations collected in Hurricanes Ian and Fiona (2022) was sufficient to establish a regime change in the primary wind speed dependence of mss, from linear growth to saturation, it was unable to reveal any concrete relationships that explained spread at a given wind speed (J. Davis et al., 2023). This was likely due to the sparsity of simultaneous observations on both sides of the storm. Understanding variation in mss at a given wind speed may help to explain changes in the spectral tail and underlying wavefield, and thus wave-induced drag within hurricanes. These observations are also useful for wave model validation and improvement within hurricanes (Reichl et al., 2014).

Section 2 provides an overview of the conditions within Hurricane Idalia and describes the free-drifting wave buoys used to estimate mss and the forecast model used to estimate 10-m winds. Section 3 presents the results and Section 4 connects the results to recent studies related to the dependence of drag coefficient on wind-wave alignment. Section 5 concludes.

Buoy observations used in this work fundamentally measure in the frequency domain, whereas mss is a spatial property dependent on k through Equation 1. This necessitates switching between wavenumber and frequency

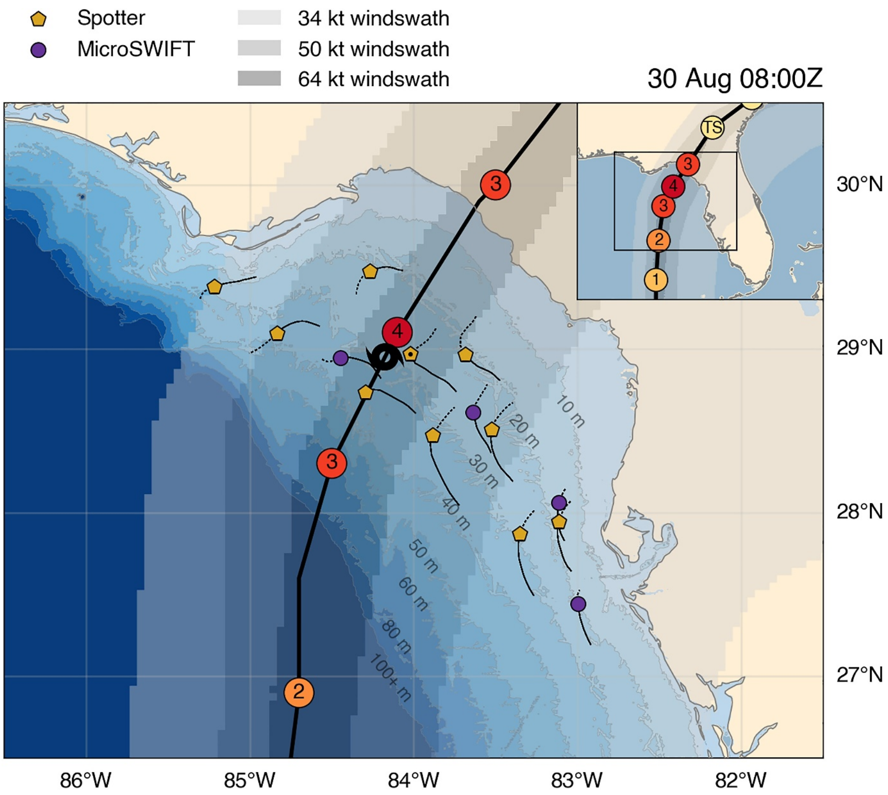

Figure 1. Wave buoys in Hurricane Idalia (2023). The hurricane symbol represents Idalia's position at 30 August 0800Z, and markers represent buoy positions at this time. Drift tracks over a 15-hr period on 30 August, used later to produce storm-following visualizations, are shown as thin black lines. Track lines are solid up to the position shown (0000Z to 0800Z) and dashed beyond (0800Z to 1500Z). The Spotter buoy nearest to the storm center (SPOT-30103D), indicated with a dot at its center, is used in the representative time series shown in Figure 2. Idalia's intensity on the Saffir-Simpson Hurricane Wind Scale is indicated inside the circles along the track, and shaded regions represent the extent of the 34, 50, and 64 knot wind swaths. Bathymetry contours are constructed from the 2023 GEBCO grid. The inset map in the upper right corner shows Idalia's track in the larger context of the Florida Gulf coast.

domains often throughout the methods, results, and discussion. As a general rule, physics will be described in the wavenumber domain (especially as related to mss), whereas observations will be described in the frequency domain.

2. Methods

This section describes wave observations and model-simulated winds in Hurricane Idalia used to study the dependence of mss on wind-wave alignment in a storm-following reference frame. We first provide an overview of wind and wave conditions in Hurricane Idalia and the storm's meteorological characteristics. Next, we describe specifications of the microSWIFT and Spotter buoys and their spectral processing methods, followed by details on buoy mss calculation and a surface drift Doppler adjustment applied to remove the effect of windage on Spotter mss estimates. We then describe the COAMPS-TC model used to produce wind fields and the process of transforming the buoys into a storm-following reference frame based on the model's forecasts and ancillary Best Track data. This section concludes with the definition of wind-wave alignment used throughout the results.

2.1. Hurricane Idalia

Hurricane Idalia made landfall as a category 4 hurricane in the Florida Big Bend region on 30 August 1145 UTC (Cangialosi & Alaka, 2024). Two days prior, a P-3 aircraft operated by the U.S. Naval Research Laboratory's Scientific Development Squadron (VXS-1) deployed an array of drifting wave buoys on both sides of the storm's forecasted path (Figure 1). At the time of Idalia's closest approach to the buoys, approximately 0800Z on 30 August, the array spanned the Big Bend coastline with most buoys 50–120 km offshore. Water depth along buoy

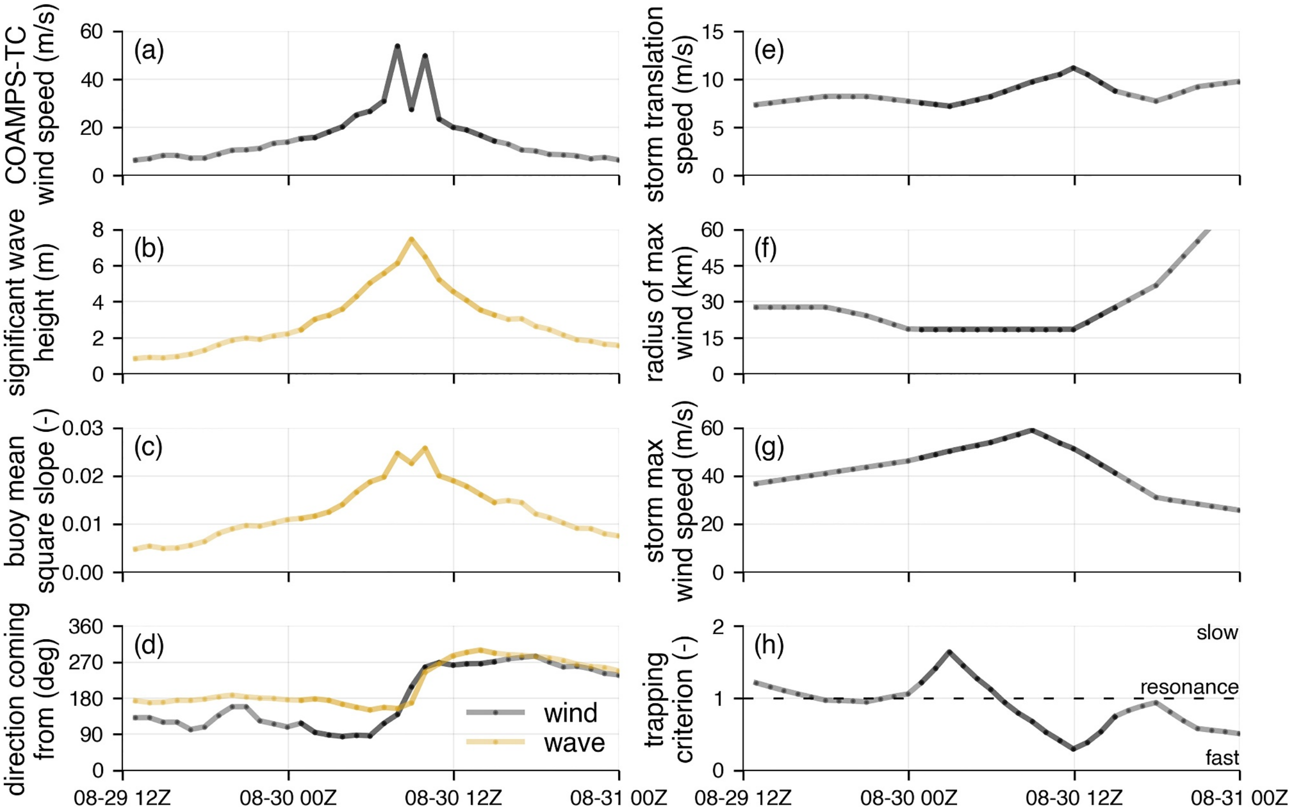

Figure 2. Time series of a representative buoy (SPOT-30103D, dotted in Figure 1) and Idalia's meteorological metrics over a 36-hr period: (a) COAMPS-TC wind speed; (b) buoy-measured significant wave height; (c) buoy-measured mean square slope; (d) buoy-measured energy-weighted wave direction and COAMPS-TC wind direction (at the buoy's position); (e)–(g) storm translation speed, radius of maximum wind, and maximum wind speed (all as reported by IBTrACS); and (h) Kudryavtsev et al. (2021) trapping criterion (ratio of dimensionless radius of maximum wind to critical fetch, their Equation 16). Idalia made landfall close to 12Z on 30 August. Wave heights peak as the storm passes closest to the buoy. The bold regions correspond to the time period shown in the storm-following reference frame.

trajectories varied within the 10–40 m depth contours, as indicated by the 2023 General Bathymetric Chart of the Oceans (GEBCO) (GEBCO Bathymetric Compilation Group, 2023). Using a relative depth metric weighted by energetic wavelengths of the spectrum, 53% of observations are in intermediate relative depths ($\pi/10 < kh < \pi$) and 47% are in deep water ($kh \geq \pi$). The maximum significant wave height recorded by the array was 7.5 m at a peak period of 12.8 s, and the maximum COAMPS-TC 10-m wind speed at a buoy's location was 52 m s^{-1} (Figures 2a–2d).

During the 24-hr period ahead of landfall, Idalia's translation speed increased from 7 to 11 m s^{-1}, radius of maximum wind (RMW) decreased from 28 to 19 km, and max 1-min averaged, 10-m wind speed intensified from 36 to 50 m s^{-1} (Figures 2e–2g). Storm metrics are from the International Best Track Archive for Climate Stewardship (IBTrACS) (Gahtan et al., 2024; Knapp et al., 2010). The Kudryavtsev et al. (2021) criterion for wave trapping, or "resonance" between the group velocity and storm translation speed, suggests the storm was too slow to reach resonance on approach to the buoy array until about 06Z on 30 August, beyond which the ratio dropped below unity (faster than resonance) until landfall (Figure 2e). The period of time when the trapping criterion crosses through unity coincides with the storm's closest approach to the array.

2.2. Wave Measurements

Surface wave measurements are from two types of free-drifting buoys: the UW-APL microSWIFT and the Sofar Spotter. Both buoys use GPS-derived velocities to estimate hourly records of surface wave statistics in the form of scalar energy spectra, $E(f)$, and directional moments, a_1, b_1, a_2, b_2 (Herbers et al., 2012).

The microSWIFT is a small and expendable wave buoy designed for aerial deployment from the A-sized dropsonde chute of research aircraft (Thomson et al., 2023). The buoy has a 45.7 cm (18 in) long, 8.9 cm (3.5

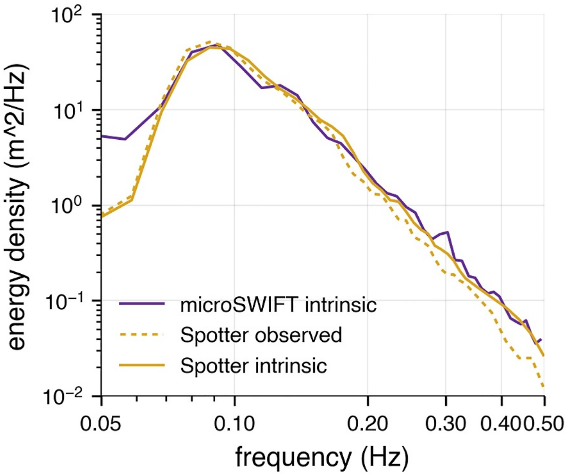

Figure 3. Comparison of intrinsic (Doppler shift adjusted) and observed energy spectra in 35 m s^{-1} winds. After adjustment for Doppler shift due to both wind slip and Stokes drift, Spotter mss calculated from the spectra shown here increased by 31%, from 0.016 (observed) to 0.021 (intrinsic). The intrinsic spectrum reported by a nearby (33 km away) microSWIFT, adjusted only for Stokes drift, is shown for comparison. In contrast, microSWIFT mss increased only 10%, from 0.020 (observed, not shown) to 0.022 (intrinsic). At this time instance, the percent difference between the Spotter and microSWIFT slopes reduced from 22% (observed) to 5% (intrinsic).

in) diameter cylindrical hull and a mass of 2.4 kg. A specialized float collar provides additional buoyancy and hydrodynamic damping. In still water, the hull has 3.5 inches of freeboard. Every hour, GPS velocities are sampled at 5 Hz for 30-min and are processed into spectra using 256-s windows with 75% overlap. Each window is high-pass filtered using a cutoff frequency of 0.04 Hz. After band merging every three adjacent frequencies, the spectra have 48 degrees of freedom and span 0.0098–0.490 Hz in 42 frequency bins. Wave energy density at the first 39 frequencies is estimated from the horizontal GPS velocities (north-south and east-west components), whereas the remaining 3 highest frequencies, which span 0.466–0.490 Hz, are estimated from the vertical GPS velocities to prevent motion contamination from the buoy's pitch (or roll) natural frequency within these bands. The buoy's heave natural frequency, 0.74 Hz, is above the highest reported frequency. Energy density, directional moments, and the mean geospatial coordinates within the hour are transmitted via Iridium.

The Spotter is a small and versatile solar-powered buoy which is deployed here in a free-drifting format (Raghukumar et al., 2019). Spotters used in this project were specially rigged for air-deployment out of the P-3 aircraft's open door (Dorsay, Houghton, et al., 2023). The sphere-like hull is 38 cm in diameter with a mass of 5.5 kg. GPS velocities are sampled at 2.5 Hz and are processed into 256-sample FFTs to produce hourly spectra spanning 0.0293–0.5 Hz in 38 frequency bins. The spectral estimates have a frequency resolution of $\Delta f = 2.5/256$ Hz up to the 0.33 Hz bin and a coarser, $3\Delta f$ resolution above this frequency to reduce the size of the Iridium message. In addition to wave measurements, Spotter buoys were also equipped with barometers and water temperature sensors. Spotter wave spectra can be used to derive proxy wind observations from the equilibrium range of the tail (Dorsay, Egan, et al., 2023), however this method is not used in the current work.

2.3. Buoy Mean Square Slope

Mean square slope is estimated using Equations 1–3 integrated from $k_1 = 0.01$ rad m^{-1} to $k_2 = 1$ rad m^{-1} (wavelengths from 620 to 6 m). This corresponds to frequencies from 0.05 to 0.5 Hz, in deep water. These frequencies contain the high energy gravity waves and typically include the spectral peak and the start of the tail (in moderate wind conditions). The upper limit of 1 rad m^{-1}, or 0.5 Hz, means waves shorter than 6 m cannot be resolved and included in the mss. Some publications refer to an mss calculated over a truncated frequency range as a "band-pass" or "low-pass filtered" mss (Hwang, 2005; D. D. Chen et al., 2016, for example). Buoy-resolved mss is a fraction of total mss at moderate wind speeds (approximately 20% relative to Cox and Munk), but it remains useful as a measure of the steepness and of the shape and energy level of the equilibrium and early saturation ranges captured within the spectral tail at these frequencies (Vincent et al., 2019). The Lagrangian nature of free-drifting buoys also means they measure smoother troughs and sharper crests relative to a fixed Eulerian measurement, since buoys spend more time in wave crests and less time in troughs (Longuet-Higgins, 1986). A Lagrangian-measured mss is reduced relative to an Eulerian-measured mss, though this effect should be order $(ak)^2$ and thus less than 1%.

2.4. Surface Drift Doppler Adjustment

A platform that is moving relative to waves experiences a Doppler shift which causes measurements made in the platform's *observed* reference frame to deviate from the reference frame that is *intrinsic* to the waves (Collins et al., 2017; Colosi et al., 2023; Amador et al., 2023, and references therein). Free-drifting buoys are nearly Lagrangian surface-following platforms, however drift components due to Stokes drift and windage (i.e., wind slip) can cause buoys to move relative to the intrinsic wave reference frame (Iyer et al., 2022). The dispersion relationship used to connect frequency domain to wavenumber domain (Equation 2) is valid in the intrinsic reference frame, thus observed spectra are adjusted to the intrinsic frame prior to computing mss (Figure 3).

For spectral wave measurements made in time, the Doppler shift manifests as a modulation in frequency. Frequencies in the observed reference frame are mapped to frequencies in the intrinsic reference frame as

$$f_{\mathrm{in}} = f_{\mathrm{ob}} + \frac{Uk\cos(\theta_r)}{2\pi} \tag{4}$$

where f_{in} is frequency in the intrinsic reference frame, f_{ob} is frequency in the observed reference frame, k is the magnitude of the wavenumber vector (which is invariant between reference frames), U is the platform's speed, and θ_r is the relative heading of the platform with respect to the waves. After mapping the frequencies, the Jacobian, $df_{\mathrm{ob}}/df_{\mathrm{in}}$, is used to map the observed energy spectrum to the intrinsic reference frame

$$E_{\mathrm{in}}\left(f_{\mathrm{in}}\right) = E_{\mathrm{ob}}\left(f_{\mathrm{ob}}\right)\frac{df_{\mathrm{ob}}}{df_{\mathrm{in}}} \tag{5}$$

where E_{in} and E_{ob} are the intrinsic and observed elevation variance spectra, respectively. Equation 5 is required to conserve variance and can be estimated using finite differencing (Collins et al., 2017). Following previous Doppler adjustment procedures, the deep water linear dispersion relationship, $f_{\mathrm{in}} = \sqrt{gk}/(2\pi)$, is used with Equation 4 to obtain a quadratic equation in k. The observed frequencies are then mapped to intrinsic frequencies considering ambiguities and limits discussed in Collins et al. (2017) and Colosi et al. (2023). The Doppler shift experienced in the observed reference frame is typically largest at high frequencies (high k). Although the effect on low-order moments (e.g., significant wave height) can be minimal, differences in high-order moments between observed and intrinsic reference frames can be large.

Spotter drift relative to the surface is due to a small amount of windage (i.e., wind slip) and surface Stokes drift. MicroSWIFTs have minimal wind slip due to their low freeboard, thus any surface-relative drift is assumed to be due to Stokes drift. Spotter wind slip is estimated by comparing to microSWIFT buoys within the data set, after removing Stokes drift contributions from the mean drift speed derived from hourly GPS fixes for both buoys. Across all wind speeds in the data set, microSWIFTs have a mean drift-to-wind-speed ratio of 3.0%, which is the rule of thumb for ocean surface drift speed as 3% of the 10-m wind speed (Samelson, 2022). The mean drift-to-wind-speed ratio of the Spotters is 4.2%, which suggests the 1.2% difference is due to wind slip. This is close to the 1% wind slip estimated for the Spotter in Houghton et al. (2021) and the 1.09% mean wind slip for the similar full-sized SWIFT v4 (Iyer et al., 2022). The drift-to-wind-speed ratio for each buoy varies with wind speed, though the 1.2% difference remains nearly constant. Surface Stokes drift is calculated from the spectral integral form for intermediate water depths. The upper frequency of 0.5 Hz may result in an underestimation of the Stokes drift (Lenain & Pizzo, 2020); however Stokes drift contributions are minor relative to contributions from windage.

Platform speed relative to the surface, U, is set to the magnitude of the wind slip and surface Stokes drift vector sum. The relative heading of the platform with respect to waves, θ_r in Equation 4, is determined using a wave direction estimated from the buoy's directional moments and the surface-relative drift direction

$$\theta_r(f) = \theta_{\mathrm{wave}}(f) - \theta_{\mathrm{drift}} \tag{6}$$

here θ_{wave} is a smoothed, frequency-dependent wave direction calculated from energy-weighted directional moments, $a_1(f)$ and $b_1(f)$, in sliding windows of 7 frequency bands. Surface-relative drift direction, θ_{drift}, is set to the direction of the Stokes drift and wind slip vector sum. The direction of the Stokes drift vector is calculated from buoy directional moments, and the direction of the wind slip vector is the direction of the wind. This direction is generally aligned with the mean drift estimated from hourly GPS fixes. Both θ_{wave} and θ_{drift} are in the "going to" convention.

The Doppler adjustment procedure relies on the validity of the deep water dispersion limit and the assumption that effects of current shear are minimal. Although longer waves in the spectrum are in intermediate water depths for more than half of the observations in the data set, all observations have an mss-weighted relative depth that indicates shorter waves are in deep water. These correspond to the high frequencies which determine mss and are subject to the largest Doppler shift, such that the deep water assumption remains valid. These short waves have a small vertical distribution of wave motion such that they effectively experience surface currents (Zippel & Thomson, 2017).

2.5. COAMPS-TC Surface Winds

Surface wind estimates are from real-time operational forecasts of Hurricane Idalia made by the U.S. Naval Research Laboratory's (NRL) Coupled Ocean-Atmosphere Mesoscale Prediction System for Tropical Cyclones (COAMPS-TC) (J. Doyle et al., 2012; J. Doyle et al., 2014). Real-time COAMPS-TC forecasts use a nested grid system with initial and boundary conditions from the NOAA Global Forecast System (GFS). When initial storm intensity is greater than 28.3 m s^{-1} (55 knots), the initial horizontal wind structure is generated from a modified Rankine wind vortex based on physical and synthetic observations from the National Hurricane Center. Below this intensity, the initial vortex is downscaled from the NOAA GFS analysis.

Surface winds (10-m reference height) from the inner-most 4-km grid are aggregated from sequential short-range real-time operational forecasts to produce "reforecast" wind fields. The first hour of each forecast is omitted to minimize the effect of model state adjustments that occur early in each forecast. Lead times of successive forecasts span 1–6 hr. Reforecast fields are adjusted from original operational forecast fields such that the maximum 10-m wind speed matches the NHC final Best Track intensity and the minimum sea-level pressure matches the NHC final Best Track minimum sea-level pressure. Surface winds, output every 15 min starting at the top of each hour, are interpolated onto wave buoy observations using bilinear interpolation in space and time.

Hurricane Idalia COAMPS-TC wind speeds are validated using Stepped Frequency Microwave Radiometer (SFMR) observations collected from 29 August to 30 August. The distribution of COAMPS-TC wind speed errors, created from $n = 1,289$ comparisons, has an estimated bias of 2 m s^{-1} and an error of 6 m s^{-1} over all wind speeds (see Appendix B). This error is nearly equivalent to the 7 m s^{-1} uncertainty used previously in J. Davis et al. (2023), estimated by comparing COAMPS-TC 6-hr intensity errors to the National Hurricane Center Best Track re-analysis across hundreds of major hurricane forecasts. Error grows as approximately 22% of wind speed. There is no discernible bias across storm quadrants.

COAMPS-TC wind direction is compared with observations from National Data Buoy Center (NDBC) Station 42036 moored at (28.501 N, 84.508 W). Station 42036 was approximately 10 km from Idalia's center on 30 August 06Z. COAMPS-TC wind direction is estimated to have a bias of $-6°$ and an error of $19°$, as estimated from a distribution of wind direction differences created from $n = 282$ comparisons to 10-min observations over 29 August 00Z to 31 August 00Z (see Appendix B). The validation of COAMPS-TC Wind speed and direction against SFMR and NDBC Station 42036 is described further in Appendix B.

2.6. Storm-Following Reference Frame

The density of buoys in the Hurricane Idalia data set enables visualization of wave measurements in a storm-following reference frame (Schönau et al., 2024, for example). To transform observations into the storm-following reference frame, the hourly position of each buoy relative to the storm center was determined using Best Track storm positions from IBTrACS. Storm positions (reported every 3 hr) were interpolated onto buoy observation times and used to compute northings and eastings relative to the storm center.

During some hours, the COAMPS-TC reforecast track (as determined by the minimum pressure) deviated from the Best Track. Since interpolation of 10-m wind speed at buoy observations close to the storm center is sensitive to errors in track, COAMPS-TC longitude-latitude grids were reprojected onto an x-y grid (centered on the storm and measured in meters) using a transverse Mercator projection. The position of each buoy relative to the IBTrACS Best Track was then translated onto this grid, and translated positions (now relative to COAMPS-TC) were used to extract 10-m wind vectors from the model x-y grid. The buoys were sufficiently offshore such that this adjustment did not translate any of them onto land, which would result in an inaccurate wind speed.

2.7. Definition of Wind-Wave Alignment

Directional alignment between wind and waves (wind-wave alignment) is calculated using COAMPS-TC 10-m wind direction and bulk wave direction measured by the buoys. A goal of this work is to understand the influence of longer, energetic waves on mss. Wind-wave alignment is thus calculated using an energy-weighted wave direction from the buoy's energy-weighted directional moments (Kuik et al., 1988)

$$\theta_{\mathrm{wave}} = \left(270^\circ - \frac{180^\circ}{\pi}\arctan2(\overline{b}_1, \overline{a}_1)\right) \bmod \; 360^\circ \tag{7}$$

where

$$\overline{a}_1 = \frac{\int a_1(f)E(f)df}{\int E(f)df} \qquad \overline{b}_1 = \frac{\int b_1(f)E(f)df}{\int E(f)df} \tag{8}$$

and $a_1(f)$ and $b_1(f)$ are the first two directional moments, which represent wave motion along the N-S and E-W principle axes at each frequency, respectively (Thomson et al., 2018). An energy-weighted direction characterizes a similar region of the spectrum as peak direction, but it is more stable in cases when there is not a well-defined peak, or when there are multiple peaks. Wind-wave alignment is defined here as the smallest angle resulting from a difference between the wind and wave directions

$$\Delta\theta = \begin{cases} \theta_{\mathrm{wind}} - \theta_{\mathrm{wave}}, & \text{if } -180^\circ \le \theta_{\mathrm{wind}} - \theta_{\mathrm{wave}} \le 180^\circ \\ \theta_{\mathrm{wind}} - \theta_{\mathrm{wave}} - 360^\circ, & \text{if } \theta_{\mathrm{wind}} - \theta_{\mathrm{wave}} > 180^\circ \\ \theta_{\mathrm{wind}} - \theta_{\mathrm{wave}} + 360^\circ, & \text{if } \theta_{\mathrm{wind}} - \theta_{\mathrm{wave}} < -180^\circ \end{cases} \tag{9}$$

or more concisely as

$$\Delta\theta = (\theta_{\mathrm{wind}} - \theta_{\mathrm{wave}} + 180^\circ \bmod \; 360^\circ) - 180^\circ \tag{10}$$

where θ_{wind} and θ_{wave} are in the "going to" convention and mod is the modulo operation. This definition ensures, for example, that wind heading toward 0° (north) and waves heading to 270° (west) results in an alignment of 90° and not −270°. Signed wind-wave alignment is $\in [-180^\circ, 180^\circ]$. Wind-wave alignment can also be thought of as the wave heading relative to wind direction.

3. Results

3.1. Spatial Distribution of Wind and Waves

Observations from the array over a 15-hr period, from 00:00Z to 15:00Z on 30 August, are transformed into a storm-following reference frame to visualize their spatial distribution within Idalia (this time period is emboldened in Figure 2). Buoy positions (1-hr apart) are normalized by the storm's radius of maximum wind, which is nearly constant at 18.5 km (10 nmi) over the period (Figure 2f). The 34-knot and 50-knot 10-m wind speed swaths, as indicated by COAMPS-TC and the Best Track wind radii, extend further to the right side of the storm (Figure 4a). Buoy-measured mss is generally highest closest to the storm center due to the dependence of mss on wind speed (Figure 4b).

The absolute wind-wave alignment ($|\Delta\theta| \in [0^\circ, 180^\circ]$) is smallest to the right and rear of the storm's center (Figure 4c). Wind and waves are less aligned toward the right-front, and are the least aligned on the left side of the storm, with most observations on the left side spanning 90° to 135° alignment. Wind-wave alignment can be categorized using definitions proposed by Holthuijsen et al. (2012) and used to describe regions in which long period waves and locally generated short period waves, and thus the wind direction, are *aligned*, *crossing*, or *opposing*:

- *aligned*: long period waves traveling within 45° of the wind; $|\Delta\theta| \in [0^\circ, 45^\circ]$
- *crossing*: long period waves traveling within 45° from the normal to the wind; $|\Delta\theta| \in (45^\circ, 135^\circ]$
- *opposing*: long period waves traveling within 45° from the opposing wind direction; $|\Delta\theta| \in (135^\circ, 180^\circ]$

(Note that the original category "following" has been renamed to "aligned").

In the storm-following reference frame, the aligned wind and waves are concentrated mostly in the right-rear quadrant of the storm, extending slightly into the right-front quadrant (Figure 5a). The remaining observations surrounding the storm are categorized by crossing wind and waves. Opposing wind and waves are only observed

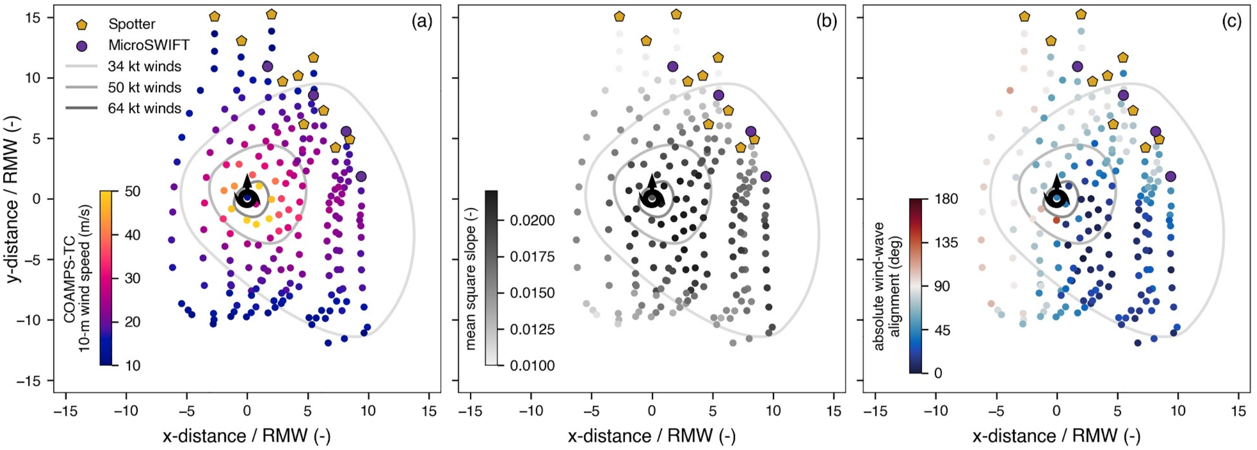

Figure 4. (a) COAMPS-TC 10-m wind speed, (b) mean square slope, and (c) absolute wind-wave alignment in a storm-following reference frame over a 15-hr period in Hurricane Idalia (2023). The initial position of each buoy is indicated by the markers with subsequent observations each spaced an hour apart. The storm center (minimum pressure) is at $(0, 0)$, and the storm heading is always in the direction of the y-axis (up). All distances are normalized by the radius of maximum wind (RMW) at each observation time. The concentric rings provide a visualization of the spatial structure of the storm and represent the approximate extent of 34 knot (17.5 m s^{-1}) tropical storm force, 50 knot (25.7 m s^{-1}) storm force, and 64 knot (32.9 m s^{-1}) hurricane force winds from the NHC Best Track. The rings are drawn by connecting the radii at each wind speed (reported for each quadrant and averaged over the 15 hr period) with arcs.

once, to the rear of the storm and at a distance of 2 RMW from the center. A distinct spatial structure in wind-wave alignment has been reported by numerous authors, though the location of the aligned waves varies between the right-front (Holthuijsen et al., 2012; Schönau et al., 2024) and right-rear quadrant of the storm (Arakawa, 1954; Hu & Chen, 2011; Tamizi & Young, 2020). In many cases, the use of wind-wave alignment to describe a hurricane wavefield can be more effective than the traditional use of quadrants (Zhou et al., 2022).

3.2. Dependence of Mean Square Slope on Wind-Wave Alignment

Buoy-derived mss is approximately linear as a function of 10-m wind speed up to 20 m s^{-1}, but approaches quasi-saturation at the highest wind speeds (Figure 5b), as described by J. Davis et al. (2023). A hyperbolic tangent fit to the data is

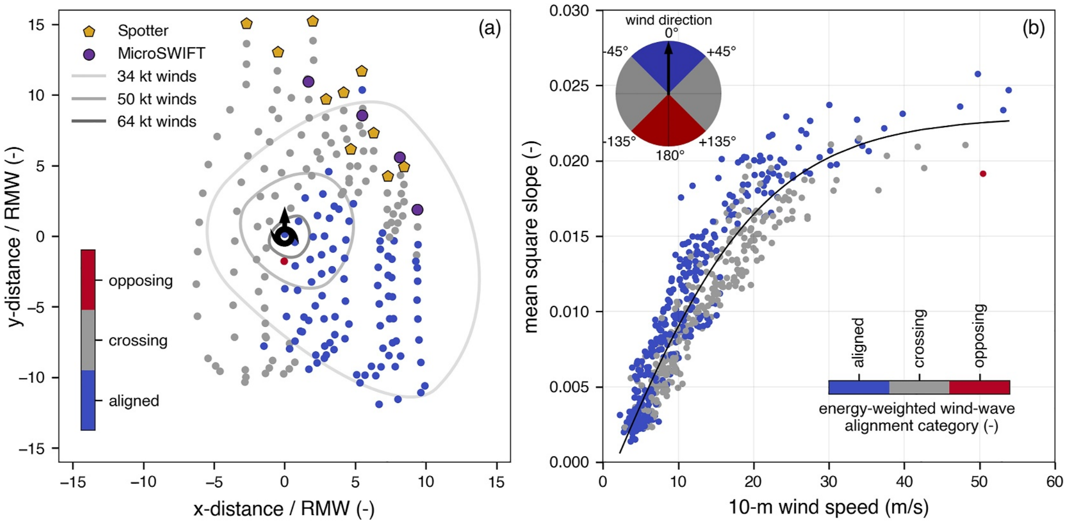

Figure 5. (a) Wind-wave alignment categories in the storm-following reference frame and (b) buoy mean square slope versus COAMPS-TC 10-m wind speed, classified by wind-wave alignment using an energy-weighted wave direction. The overall fit, Equation 11, is shown in (b). The legend in the upper left corner of (b) shows the definition of the alignment categories based on the wave direction (azimuth) relative to the wind direction (black arrow at 0°).

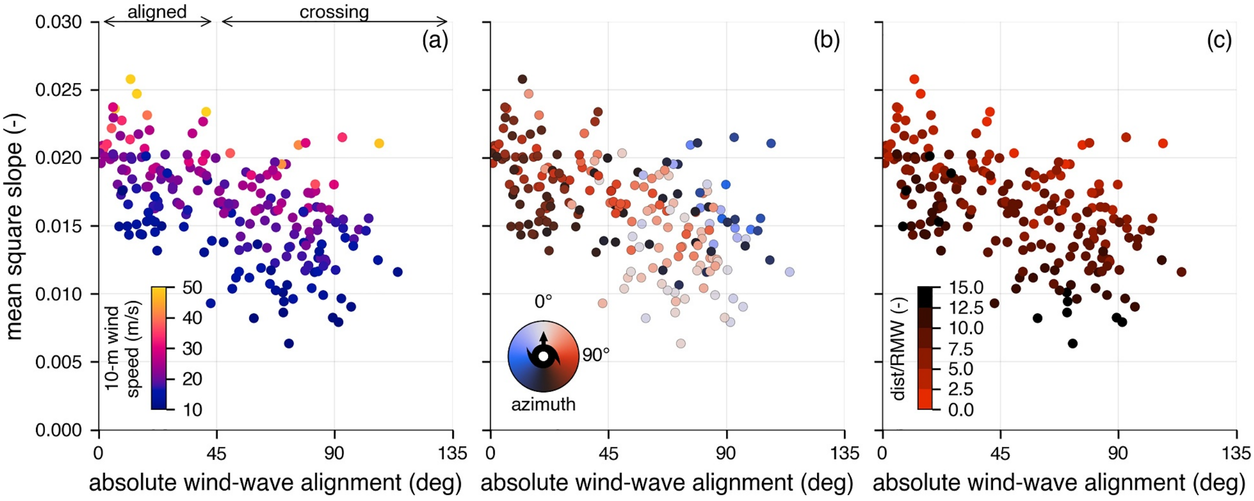

Figure 6. Mean square slope versus absolute wind-wave alignment classified by (a) 10-m wind speed, (b) azimuth, and (c) RMW-normalized distance relative to the center of the hurricane. The color map used in (b) is cyclic with red points corresponding to observations on the right side of the storm and blue points corresponding to observations on the left side.

$$\mathrm{mss} = a \tanh(bU_{10}) + c \tag{11}$$

with $a = 0.0250 \pm 0.0009$, $b = 0.0476 \pm 0.0040$ $(\mathrm{m/s})^{-1}$, and $c = -0.0020 \pm 0.0006$ where uncertainties represent 95% confidence intervals on the parameters derived from the covariance matrix estimated during the nonlinear least squares fitting. The root mean square error of the fit is 0.0020. Equation 11 is valid for $U_{10} \in [2, 52]$ m s^{-1} and for an mss integrated from $k_1 = 0.01$ rad m^{-1} to $k_2 = 1$ rad m^{-1} (wavelengths from 620 to 6 m). Despite the asymptotic nature of tanh as $U_{10} \to \infty$, mss at these scales is not expected to asymptote completely, since a spectrum dominated by the saturation range has a nonzero contribution to mss (though the increase in slope with wind speed is drastically reduced).

When separated by wind-wave alignment, mean square slopes corresponding to aligned wind and waves have positive residuals (observations minus fit), generally sorting above the fit for wind speeds exceeding 5 m s^{-1}. Where wind and waves are crossing, mss tends to lie below the fit (negative residuals). Individual fits of Equation 11 to categorized mss indicate the parameter a is unique to each category (the remaining parameters are contained within confidence intervals of the other category's fit). Treating wind-wave alignment as a categorical variable, a multivariate fit to the categorized data is

$$\mathrm{mss}(U_{10}, \Delta\theta) = (a + a' \mathbf{1}_{\mathrm{aligned}}(\Delta\theta)) \tanh(bU_{10}) + c \tag{12}$$

where $\mathbf{1}_{\mathrm{aligned}}(\Delta\theta)$ is an indicator function which evaluates to 1 if $\Delta\theta$ is categorized as "aligned" and evaluates to 0 if $\Delta\theta$ is categorized "crossing" such that

$$\mathrm{mss}(U_{10}, \Delta\theta) = \begin{cases} (a + a') \tanh(bU_{10}) + c, & 0^\circ \le |\Delta\theta| \le 45^\circ \text{ (aligned)} \\ a \tanh(bU_{10}) + c, & 45^\circ < |\Delta\theta| \le 135^\circ \text{ (crossing)} \\ \text{not observed} & 135^\circ < |\Delta\theta| \le 180^\circ \text{ (opposing)} \end{cases} \tag{13}$$

With $a = 0.0236 \pm 0.0007$, $a' = 0.0037 \pm 0.0005$, $b = 0.0502 \pm 0.0035$ $(\mathrm{m/s})^{-1}$, and $c = -0.0028 \pm 0.0006$ with a root mean square error of 0.0018. The approximate 95% confidence interval on a', $[0.0032, 0.0042]$ does not contain zero, which suggests this parameter, and thus the impact of alignment on the fit, is statistically significant (Figure 9a). Only one observation falls into the "opposing" wind-wave alignment category such that the behavior of mss within this category is unknown.

The inverse dependence of mss on wind-wave alignment is strongest on the right side of the storm and away from the storm center (Figure 6). Some observations within a distance of approximately 2.5 times the RMW (2.5 × 18.5

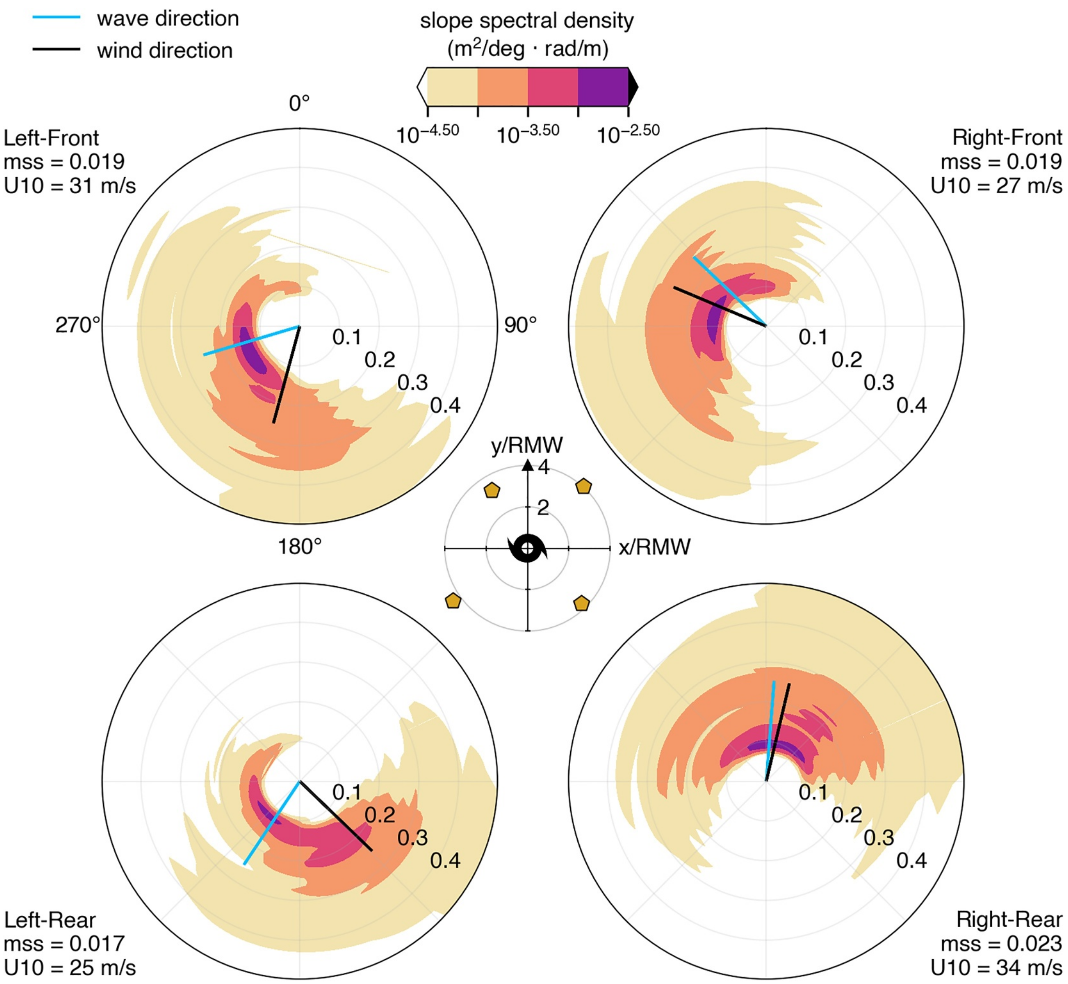

Figure 7. Example directional slope spectra in each of the four quadrants. In each plot, the azimuth indicates the direction of the energy and frequency increases radially outward (frequencies are shown as mapped from their corresponding wavenumber via the dispersion relation). All directions are in the "going to" convention and 0° is aligned with the hurricane's heading. The center panel shows the position (in RMW-normalized coordinates) of each buoy relative to the hurricane's center.

km, or 46 km) from the center may have high mss, even when the wind-wave alignment is large. This is likely because wind and wave directions can vary rapidly over short distances close to the center of the storm (Holthuijsen et al. (2012) remove observations inside a 30 km radius for a similar reason). Further from the center, but still within the radius of 50 knot (25.7 m s^{-1}) winds, mss is 2–3 times higher when the wind and waves are aligned compared to when the wind and waves crossing (Figure 6). The variance in mss increases with increasing absolute alignment.

3.3. Spatial Distribution of Slope Spectra

The dependence of mss on wind-wave alignment suggests energy levels in the spectral tail and steepness are amplified in certain regions of the storm. The slope spectrum describes the contribution of each wavelength and direction to mss

$$S(k,\varphi) = k^2 E(k,\varphi) \tag{14}$$

Where φ is spectral wave direction. To compute slope spectra from buoy observations, directional energy density spectra, $E(f,\varphi)$, are estimated from the Maximum Shannon Entropy Method (MEM-II) and converted to the wavenumber domain, $E(k,\varphi)$, using Equation 3 (Christie, 2024; Kobune & Hashimoto, 1986). A comparison of directional slope spectra with wind and wave directions by storm quadrant is shown for four representative buoys

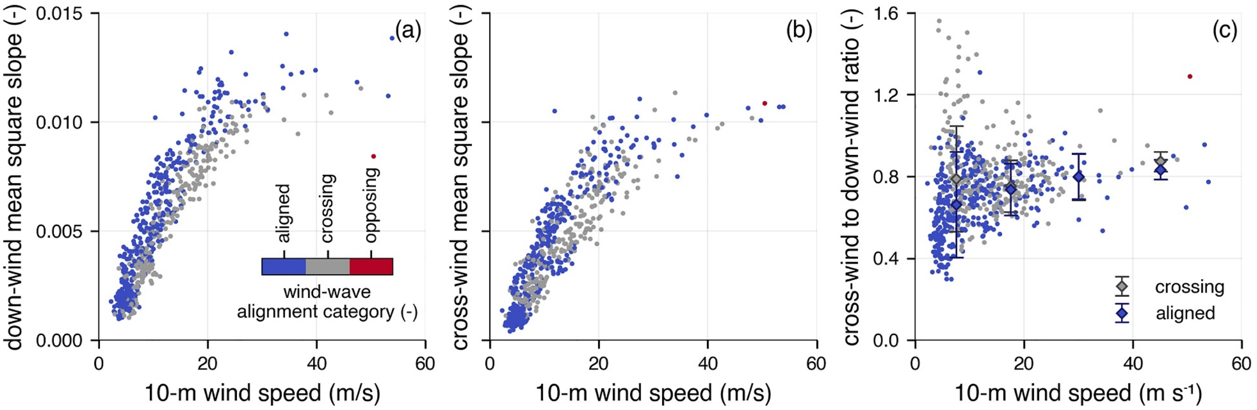

Figure 8. Mean square slope components: (a) Down-wind (mss_{down}), (b) cross-wind ($\text{mss}_{\text{cross}}$), and (c) cross-wind to down-wind ratio, all versus 10-m wind speed and classified by wind-wave alignment using an energy-weighted wave direction.

in Figure 7. Observations in each quadrant are from unique buoys between 2 RMW and 4 RMW from Idalia's center and are collected within a three-hour span.

Where wind and waves are aligned, the highest energy at each frequency in the slope spectrum is concentrated along the same direction and slopes are elevated. At these wind speeds, the highest frequencies are dominated by the f^{-5} $\left(k^{-3}\right)$ saturation range, thus energy levels in slope spectra decay (as f^{-1}) as the frequency increases (Figure A2). The wind-wave alignment dependence means mss can be substantially higher in aligned conditions compared to crossing conditions, even if wind speeds are comparable. This is the case in Figure 7: in the right-rear quadrant $U_{10} = 34$ m s^{-1}, $|\Delta\theta| = 10°$, and mss $= 0.023$ compared to the left-front with $U_{10} = 31$ m s^{-1}, $|\Delta\theta| = 54°$, and mss $= 0.019$. The percent difference in mss across quadrants is 19%. In contrast, evaluating the fit to all data in Equation 11 (primary wind speed dependence) at these wind speeds predicts only a 5% difference (mss = 0.020 to mss = 0.021) (However, these wind speeds fall within the 7 m s^{-1} uncertainty estimated for high wind regions in COAMPS-TC).

3.4. Down-Wind and Cross-Wind Mean Square Slope

Down-wind and cross-wind mss components describe slope energy projected along and perpendicular to wind direction, respectively. After the directional slope spectrum is rotated such that wind direction is aligned with the positive x-axis, the down- and cross-wind mss are the components along each axis (Elfouhaily et al., 1997)

$$\text{mss}_{\text{down}} = \int_{k_1}^{k_2} \int_0^{2\pi} \cos^2(\varphi) S(k,\varphi) d\varphi dk \tag{15}$$

and

$$\text{mss}_{\text{cross}} = \int_{k_1}^{k_2} \int_0^{2\pi} \sin^2(\varphi) S(k,\varphi) d\varphi dk \tag{16}$$

where φ is defined in the mathematical convention: 0° is aligned with the positive x-axis (wind direction), directions indicate "going to", and values are measured positive counterclockwise. By definition, $\text{mss} = \text{mss}_{\text{down}} + \text{mss}_{\text{cross}}$.

Down-wind slopes are consistently higher in aligned wind and wave conditions across all wind speeds (Figure 8). Cross-wind slopes are elevated in aligned wind and waves until 30 m s^{-1}, beyond which cross-wind slopes in the aligned condition cease to increase. In contrast to the components, the ratio of cross-wind to down-wind mss, a measure of slope directionality, does not show substantial variation over most wind speeds (Figure 8c). The exceptions are at low wind speeds, where the ratio is sensitive, and at high wind speeds, where there are few data points. Bins centered on wind speeds [7.5, 17.5, 30.0, 45.0] m s^{-1} with [10, 10, 15, 15] m s^{-1} widths have medians

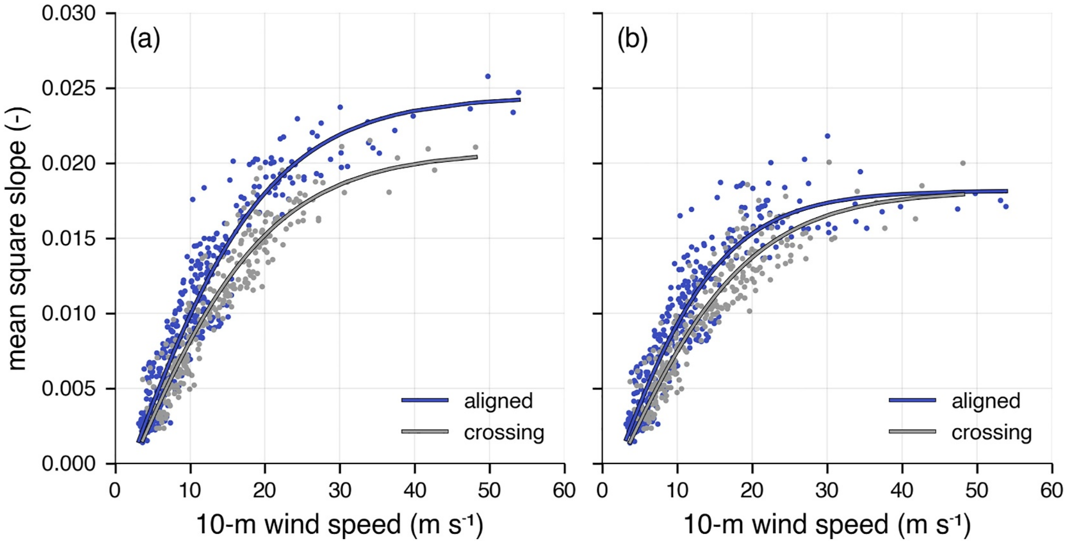

Figure 9. Aligned and crossing fit to mean square slope versus 10-m wind speed for (a) Intrinsic (Doppler-adjusted) mean square slope and (b) observed mean square slope.

± 1 standard deviation of [0.66 ± 0.17, 0.74 ± 0.11, 0.80 ± 0.11, 0.83 ± 0.11] (aligned) and [0.79 ± 0.26, 0.75 ± 0.13, 0.80 ± 0.11, 0.87 ± 0.05] m s^{-1} (crossing).

4. Discussion

4.1. Drag Coefficient and Wind-Wave Alignment

Mean square slope is enhanced in aligned conditions (low wind-wave alignment) relative to crossing conditions (moderate wind-wave alignment) as shown in Figures 5 and 6. The dependence of mss on wind-wave alignment in hurricanes is consistent with the dependence of drag coefficient on wind-wave alignment in hurricanes shown in some models (Husain et al., 2022; Manzella et al., 2024) and in some observations (S. Chen et al., 2022; Zhou et al., 2022). These studies find drag coefficient is lower in crossing conditions relative to aligned conditions. The reduction of drag coefficient with decreasing wind-wave alignment may be attributed to the reduction of long wave-induced form drag in crossing sea states (Zhou et al., 2022). Model studies have demonstrated correlation between mss and form drag (Sullivan et al., 2018), thus the dependence of both mss and drag coefficient on wind-wave alignment is plausibly related. Buoy-measured mss is only a partial representation of the spectral tail (up to 0.5 Hz or 6-m wavelength), but it captures the energetic region of the gravity wave spectrum including larger and longer waves hypothesized to steer form stress in aligned and crossing sea states, the equilibrium range, and the start of the saturation range (at moderate wind speeds).

Despite qualitative agreement between the dependence of mss and drag coefficient on alignment, based on results from the aforementioned models and observations, drag coefficient is not consistently observed to decrease in crossing wind and waves. Drag coefficients reported by Holthuijsen et al. (2012) are lower in crossing conditions than in following (aligned) conditions below 25 m s^{-1}, which agrees with the mss dependence. Above this wind speed, however, drag coefficients in crossing winds and waves greatly exceed drag coefficients in following winds and waves, which is opposite the mss dependence. A modest increase of drag coefficient in crossing conditions has also been observed outside of tropical cyclones, including behind atmospheric cold fronts embedded in extratropical cyclones (Sauvage et al., 2024). These inconsistencies suggest the dependence of drag coefficient on wind-wave alignment varies across regimes. Variation in mss dependence on wind-wave alignment across similar regimes has yet to be explored.

4.2. Generalization to Other Tropical Cyclones

The spatial pattern of wind-wave alignment is similar to that of Zhou et al. (2022) and S. Chen et al. (2022): wind and waves are aligned to the rear of the storm significantly far from the center, but are misaligned in the far right-front (beyond 2–3 × RMW) and on the left side of the storm (Figure 5a). Although this pattern is frequently reported in hurricane observations, it is not universal. Other works, for example, have reported alignment toward the right-front (Holthuijsen et al., 2012; Schönau et al., 2024).

It is likely that the strength, size, and translational speed of a hurricane shift wave directions, and thus the aligned region, within the right side of the storm due to the moving fetch phenomenon (Kudryavtsev et al., 2021). Although the self-similar solutions for wave direction derived from wave growth derived by Kudryavtsev et al. (2021) might be used with Equation 12 to produce a spatial map of mss based on storm metrics alone, the validity of the solutions is limited to waves within a radius of 3 × RMW (most observations are further from the storm due to Idalia's small RMW, Figure 5). The correlation between mss and wind-wave alignment suggests the region with elevated slopes should consistently coincide with the region of best alignment; however, conclusive evidence will require observations across several storms with varying spatial distributions of wave direction. The region of highest slopes is unlikely to be constrained by quadrant (e.g., the highest slopes may not always occur in the right-rear quadrant).

4.3. Storm-Following Reference Frame Considerations

Buoy data over a 15-hr period are used to construct the storm-following reference frame observations shown in Figures 4 and 5. Wave observations are made simultaneously in the cross-track direction, but mostly rely on the storm's progression over the array to sample in the along-track direction (although there are instances where the array spans all four quadrants at the same time, e.g., Figure 7). In the first half of this period, from 00Z to 06Z on 30 August, the maximum wind speed increased by 6 m s^{-1} (12 knots) peaking at 53.5 m s^{-1} (104 knots), whereas the array was still in the front half of the storm (Figure 2g). Past 06Z, the maximum wind speed fell by 2 m s^{-1} (4 knots) as the array was in the back half of the storm. Thus it is unlikely that storm intensification is responsible for the elevated mss in the right-rear of the storm. Although waves in the back half of the storm experience a longer duration of forcing as the storm passes, prior work suggests the response time of buoy-measured mss is between 0.4 and 1.2 hr (at 14 m s^{-1}), and that the response time decreases as wind speed increases, as the upper frequency limit increases, and as atmospheric stability decreases (D. D. Chen et al., 2016). The 1-hr spacing of the buoy observations should be sufficient for mss to respond.

4.4. Doppler Adjustment Implications

Buoy observations require an adjustment for the Doppler shift that occurs between the observed reference frame of the buoy and the intrinsic reference frame of the waves. Spotter spectra are adjusted for Doppler shift due to a 1.2% wind slip and Stokes drift, whereas microSWIFT spectra are adjusted only for Stokes drift. Spotter mean square slopes at the highest wind speeds (>30 m s^{-1}) can increase by as much as 30% after adjusting to the intrinsic frame, which indicates saturation of mss with wind speed is less acute than previously described in J. Davis et al. (2023) (see Appendix A). The dependence of mss on wind wave alignment is robust whether data are adjusted for the Doppler shift or not (Figure 9). Equation 11 fit to the observed (not adjusted) data suggests the b parameter is instead unique to each category. Using the same indicator function, this coefficient can be replaced with $b + b'\mathbf{1}_{\text{aligned}}(\Delta\theta)$ where $a = 0.0208 \pm 0.0006$, $b = 0.0530 \pm 0.0040\ (\text{m/s})^{-1}$, $b' = 0.0121 \pm 0.0023\ (\text{m/s})^{-1}$, and $c = -0.0026 \pm 0.0006$ (95% confidence intervals). The upper and lower bounds on b' are $[0.0098, 0.0144]\ (\text{m/s})^{-1}$ such that this coefficient remains statistically significant between categories when fit to observed mss. Aligned and crossing observed mss converge at high wind speeds (> 30 m s^{-1}), since the spectral tail that determines mss is significantly Doppler shifted due to wind slip.

4.5. Other Secondary Dependencies

There are several other plausible mss secondary dependencies aside from wind-wave alignment. Inverse wave age, the ratio of wind speed to the wave phase speed, is commonly used to parameterize drag coefficient (Edson et al., 2013). When calculated using phase speed at the energy-weighted wave period, inverse wave age correlates with wind speed, but does not explain variation in mss at a given wind speed (Figure 10a). Long waves steepen as they shoal and may modulate shorter waves through sheltering or increased turbulence, however there is not a distinct dependence of mss on relative depth (Figure 10b). It is possible that depth still effects mss indirectly through an increase in wind-wave misalignment as larger waves shoal, though this would require comparison to observations in deep water (X. Chen et al., 2020). Wave steepening (or flattening) can occur as waves cross

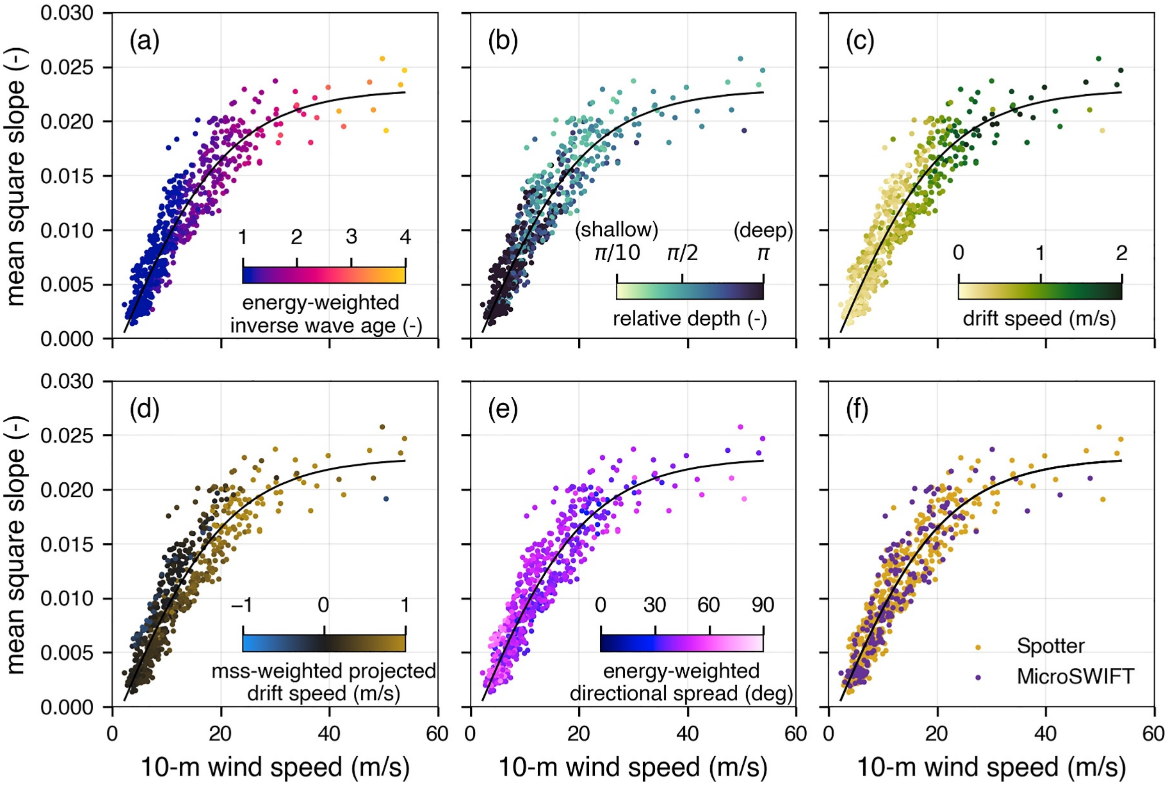

Figure 10. Mean square slope versus 10-m wind speed classified by (a) inverse wave age calculated using wave phase speed at the energy-weighted period; (b) relative water depth, or *kh*, calculated as the product of energy-weighted wavenumber and water depth; (c) buoy drift speed; (d) drift speed projected onto mss-weighted wave direction; (e) wave directional spread calculated from energy-weighted directional moments; and (f) buoy type.

surface current gradients (Iyer et al., 2022). Buoy drift speed, a proxy for surface current magnitude, increases with increasing wind speed approximately as the 3% rule of thumb, for example, Samelson (2022) (Figure 10c). When projected onto mss-weighted wave direction, projected drift speed does not elevate or lower mss as observed in Iyer et al. (2022); waves would need to be measured crossing surface current gradients for a Doppler shift of this type to be directly observed (Figure 10d). The mss-weighted wave direction used in the projected drift speed is calculated from Equation 8 with an a_1 and b_1 weighted by the fourth spectral moment and is chosen since this is the wave direction at the frequencies with the largest contribution to mss. There is not substantial variation of mss with the directional spread calculated using energy-weighted moments, though normalization of mss by directional spread was found to improve parameterizations by Banner et al. (2002) and Schwendeman et al. (2014) (Figure 10e). There is no appreciable bias introduced by buoy type (Figure 10f).

Hwang and Fan (2018) find a moderate secondary dependence on hurricane wind field asymmetry, a weaker dependence on the maximum wind speed, and little to no dependence on the radius of maximum wind speed. Several modeling and observational studies have reported variations in wind stress and drag coefficient from deep to shallow water (Jiménez & Dudhia, 2018; X. Chen et al., 2020; S. Chen et al., 2022). Variations are primarily attributed to wave shoaling, and specific trends appear to have a complex dependence on factors such as beach slope and storm translation speed. A comparison across data sets with a similar spatial density, but with varying hurricane conditions, is required to test for mss dependencies on water depth and storm strength, size, and translational speed.

4.6. Extension to Higher Wavenumbers

The primary dependence of mss on wind speed in hurricanes is consistent across measurement platforms, including radar measurements which resolve mss down to wavelengths of 0.2 m (J. Davis, Thomson, Butterworth, et al., 2024). From the present data set, it is not clear whether the secondary dependence of mss on wind-wave alignment persists down to shorter wavelengths. Future work should use methods capable of near-synoptic measurements of short-wave mss and wave direction in hurricanes to test for this dependence. Efforts to test the dependence of Wide Swath Radar Altimeter mss on wind-wave alignment are ongoing.

5. Conclusions

Mean square slope, mss, has a primary dependence on wind speed that is linear at low-to-moderate wind speeds and approaches saturation at hurricane wind speeds. Observations from an array of drifting buoys deployed inside Hurricane Idalia (2023) show mss, resolved down to 6 m wavelength, has a secondary dependence on wind-wave alignment which can help explain variation in mss at a given wind speed. Mean square slopes are higher where wind and waves are aligned than where wind and waves are crossing. This dependence is robust across all observed wind speeds, as indicated by fits to the respective categories. In the case of Idalia, slopes are elevated in the right-rear of the storm where wind-wave alignment is the closest. The dependence of mss on wind-wave alignment resembles the dependence of drag coefficient on wind-wave alignment described in recent observational and model studies (Manzella et al., 2024; Zhou et al., 2022). Form drag formulations depend on the shape and energy level within the spectral tail, both of which are reflected by changes in mss (Donelan et al., 2012). This suggests dependencies of mss and drag coefficient on wind-wave alignment are related. Future work should focus on testing this dependence with methods that can resolve wave spectra at higher frequencies inside hurricanes.

Appendix A: Doppler-Adjusted Observations

The Doppler-adjusted Hurricane Ian and Fiona (2022) data sets (prior work) are shown with the Idalia (2023) data set (current work) in Figure A1. There is little to no difference between observed and intrinsic observations below 20 m s^{-1}; however, intrinsic mss can be as much as 30% higher compared to observed mss at wind speeds exceeding 35 m s^{-1}. Intrinsic mss saturation is not as strong as previously reported; however the rate of increase in mss with 10-m wind speed is substantially reduced above 25 m s^{-1}.

When the Doppler-adjusted Idalia data are binned by 10-m wind speed (following prior work), the mean spectra remain dominated by the f^{-5} saturation range at the highest wind speeds (Figure A2). The f^{-4} equilibrium range is progressively narrowed until it is nearly absent at wind speeds exceeding 25 m s^{-1}. The increase in spectral tail steepness is directly reflected in the change in mss: an mss integrated over a largely saturated spectrum with $E(f) \sim c_s f^{-5}$ has only logarithmic contributions to mss with increasing frequency, whereas the contributions of equilibrium range with $E(f) \sim c_e f^{-4}$ are linear in frequency (c_s and c_e are constants related to the spectral energy levels).

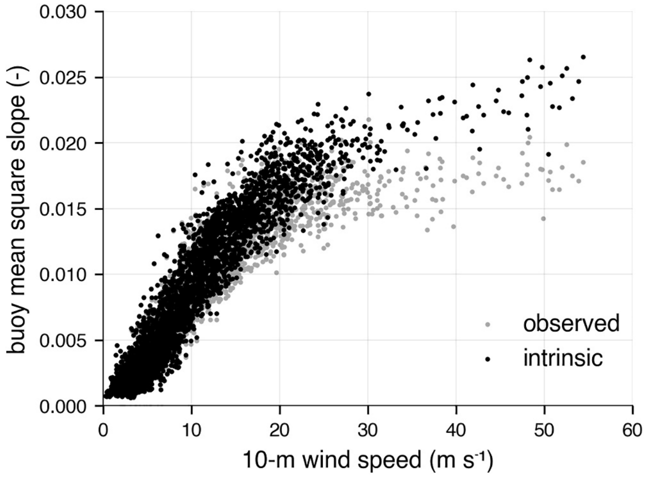

Figure A1. Observed and intrinsic mean square slope (0.05–0.5 Hz) versus wind speed. The data include observations from Hurricane Idalia (this study) and Hurricanes Ian and Fiona (J. Davis et al., 2023).

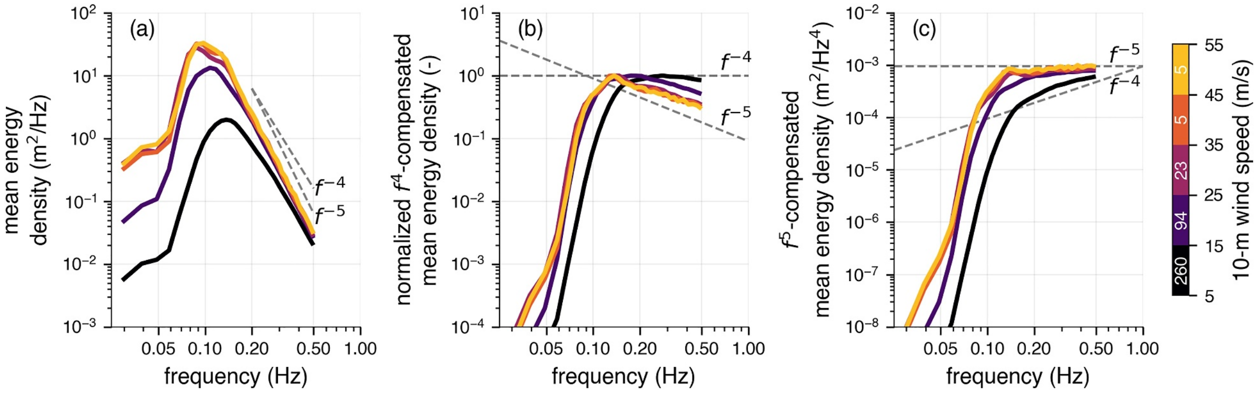

Figure A2. Hurricane Idalia Spotter spectra in 10 m s^{-1} wind speed bins: (a) mean energy density; (b) mean energy density compensated by f^4 and normalized by the maximum value in each respective bin; and (c) mean energy density compensated by f^5. Bin counts (number of 1-hr spectra) are labeled inside of the color bar.

Appendix B: COAMPS-TC Validation

Reforecast COAMPS-TC fields were validated using observations collected from 29 August to 31 August 2023. Surface wind speed SFMR observations from five missions flown by NOAA and the United States Air Force Reserve Weather Reconnaissance Squadron were colocated with COAMPS-TC using the same interpolation method used to colocate buoy observations. Stepped Frequency Microwave Radiometer observations (1 Hz) were averaged to 1-min wind speeds (COAMPS-TC outputs instantaneous values representative of a 1–10 min average).

The distribution of COAMPS-TC wind speed errors relative to SFMR, created from $n = 1{,}289$ comparisons, has a mean (bias) of 2 m s^{-1} and a standard deviation (error) of 6 m s^{-1} (Figure B1). When grouped into 10 m s^{-1} bins spanning 15 m s^{-1} to 55 m s^{-1}, error increases as 19%–24% of wind speed. Above 30 m s^{-1}, COAMPS-TC is biased high relative to SFMR (Figure B2a). A storm-centered composite of COAMPS-TC wind speed errors suggests COAMPS-TC overestimated the size of the storm near the actual RMW (Figure B2b). Most buoy observations are outside the RMW, where COAMPS-TC and SFMR are in good agreement (Figures 4 and 5). Despite an overestimation of storm size, there is little bias across storm quadrants (which might otherwise produce an erroneous mean square slope dependence on wind-wave alignment).

Hurricane Idalia passed almost directly over NDBC Station 42036 moored at (28.501 N, 84.508 W). Station 42036 was as close as 10 km to Idalia's center on 30 August 06Z. COAMPS-TC 10-m wind directions were compared with NDBC-measured wind direction, reported every 10-min at an anemometer height of 3.8 m. A distribution of COAMPS-TC wind direction errors relative to NDBC, created from $n = 282$ comparisons, has a mean of $-6°$ and a standard deviation of 19° (Figure B3). The accuracy of COAMPS-TC wind direction should be sufficient for the broad categorization of wind-wave alignment used to obtain the results (aligned, crossing, or opposing).

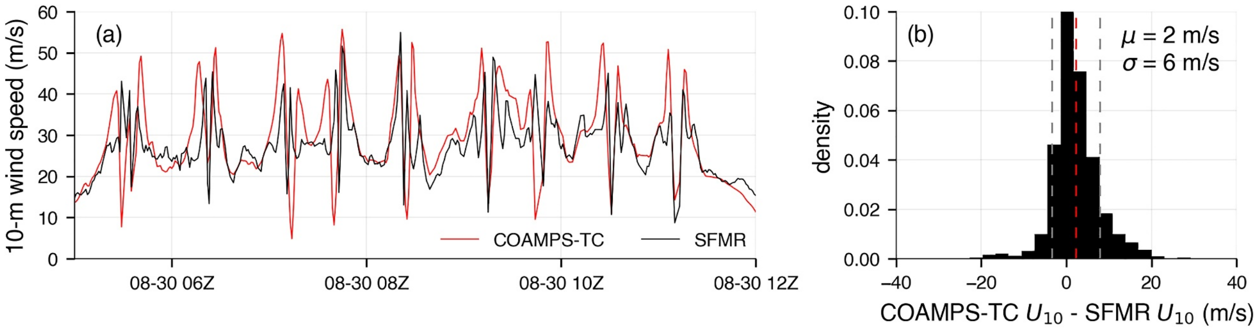

Figure B1. (a) Example time series of COAMPS-TC and SFMR 10-m wind speed. SFMR data are from mission 20230830U1 flown on 30 August. (b) Histogram of COAMPS-TC surface wind speed error, relative to SFMR surface wind speed, created from $n = 1{,}289$ total observations. Dashed lines represent the mean (red) and mean ± 1 standard deviation (gray).

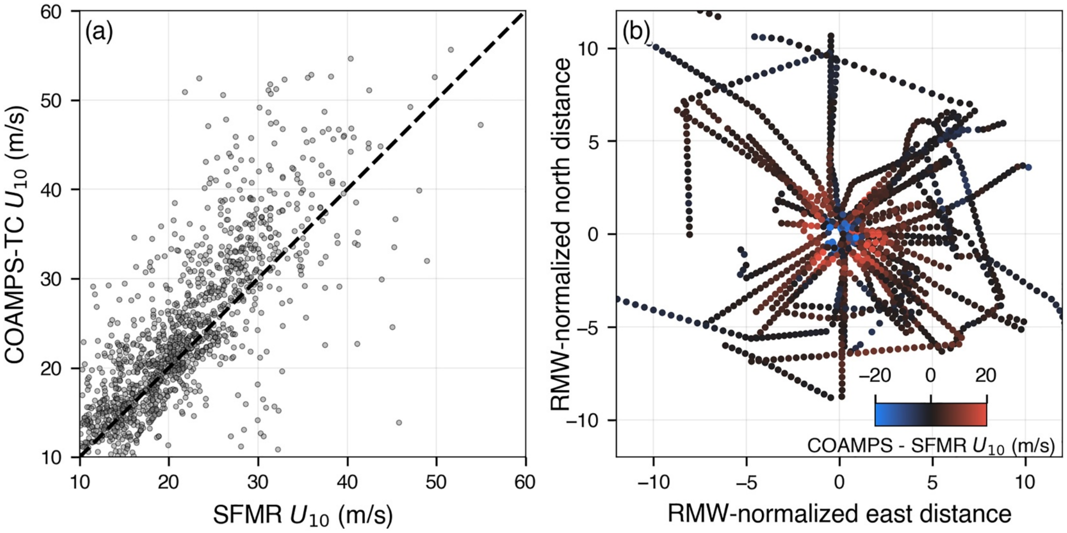

Figure B2. (a) Comparison of SFMR and COAMPS-TC surface wind speed estimates. (b) COAMPS-TC surface wind speed error in a storm-centered, RMW-normalized reference frame.

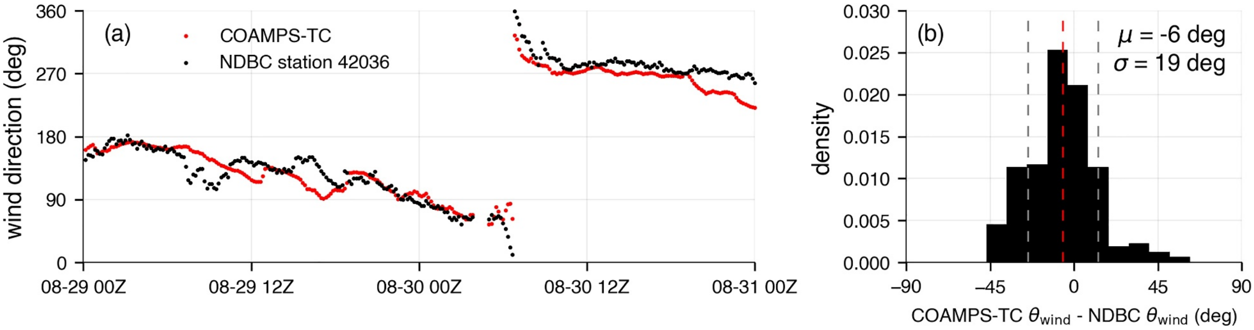

Figure B3. (a) Time series of COAMPS-TC and NDBC wind direction. (b) Histogram of COAMPS-TC wind direction error relative to NDBC wind direction. Dashed lines represent the mean (red) and mean ± 1 standard deviation (gray).

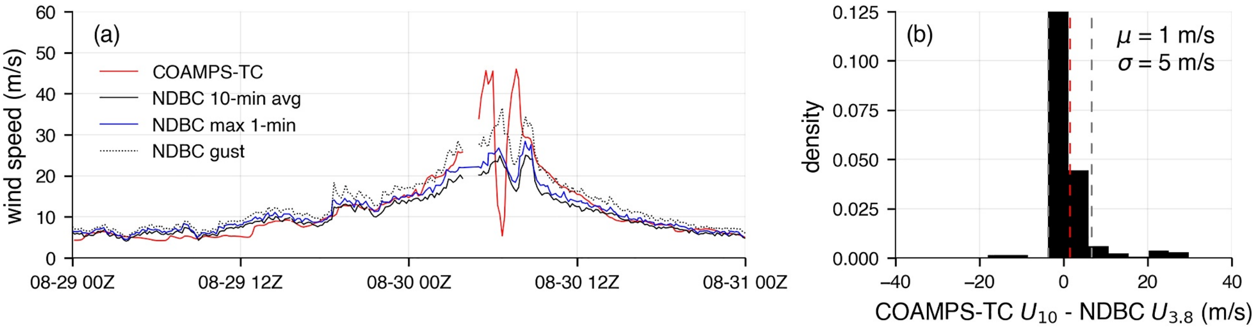

Figure B4. (a) Time series of COAMPS-TC 10-m wind speed and NDBC 3.8-m wind speed. (b) Histogram of COAMPS-TC wind speed error relative to NDBC wind speed. Dashed lines represent the mean (red) and mean ± 1 standard deviation (gray).

COAMPS-TC and NDBC Station 42036 wind speeds compare well until the buoy is inside Idalia (Figure B4). Within the storm, Station 42036 reported a maximum 10-min wind speed of 25 m s^{-1} and maximum 1-min wind speed of 28 m s^{-1} (at 3.8-m anemometer height). These observations are much lower than the maximum 10-m wind speed of 46 m s^{-1} reported by COAMPS-TC at the buoy's location (Station 42,036 recorded gusts as high as 36.5 m s^{-1} at anemometer height, though gustiness is not resolved by COAMPS-TC). The large difference in buoy-measured and modeled wind speed is unlikely to be accounted for by differences in measurement height alone. General agreement in wind speed magnitude between COAMPS-TC and SFMR (Figure B1) suggests NDBC Station 42036 is potentially unrepresentative of true 10-m wind speed during Idalia's passing. Some of this difference may be from measurement bias within the wave boundary layer (Buckley & Veron, 2016). NDBC-reported significant wave heights exceed the 3.8 m anemometer height during Idalia's entire passing (the maximum significant wave height is 6.3 m). Previous work has reported low wind measurement bias due to flow distortion over waves below 18 m s^{-1} (E. E. Wright et al., 2021); however, large differences observed here warrant investigation into sheltering effects on measured winds within hurricanes. COAMPS-TC also predicts an earlier arrival of the storm, although errors due to phase shift and storm structure should be well-captured by the SFMR wind speed error analysis.

Data Availability Statement

Data are available on Dryad (https://doi.org/10.5061/dryad.zw3r228h7) and are cited as J. R. Davis, Thomson, Houghton, et al. (2024). Source code can be accessed via GitHub (https://github.com/jacobrdavis/ocean-surface-wave-slopes-and-wind-wave-alignment-observed-in-Hurricane-Idalia) or Zenodo (https://doi.org/10.5281/zenodo.13953570) and are cited as J. R. Davis (2024). Hurricane Best Track data and storm metrics are from the International Best Track Archive for Climate Stewardship (IBTrACS) (Gahtan et al., 2024; Knapp et al., 2010). Shapefiles of the storm track and wind swaths used in the maps are from the National Hurricane Center GIS Archive available at https://www.nhc.noaa.gov/gis/. Bathymetric data are from the 2023 General Bathymetric Chart of the Oceans (GEBCO Bathymetric Compilation Group, 2023). Data from National Data Buoy Center Station 42036 (West Tampa) are available on the NDBC archive (NOAA National Data Buoy Center, 1971). Stepped Frequency Microwave Radiometer data are available at https://www.aoml.noaa.gov/2023-hurricane-field-program-data/#idalia. Colormaps are from colorCET (https://colorcet.holoviz.org/) and cmocean (https://matplotlib.org/cmocean/) (Kovesi, 2015; Thyng et al., 2016). Directional spectra are estimated using the Rogue Wave Spectrum package (https://github.com/sofarocean/oceanwavespectrum).

Acknowledgments

This work was funded by the U.S. National Ocean Partnership Program (NOPP) as part of the NOPP Hurricane Coastal Impacts project (ONR Grant N00014-21-1-2194). Air-support was provided by the Navy VXS-1 Scientific Deployment Squadron via the Naval Research Laboratory. Gijs de Boer, Brian Butterworth, Elizabeth Thompson and Chris Fairall were additionally supported by the NOAA Physical Sciences Laboratory, and the work was supported in part through NOAA cooperative agreement NA22OAR4320151, for the Cooperative Institute for Earth System Research and Data Science (CIESRDS). Co-authors Doyle and Moskaitis gratefully acknowledge support from Office of Naval Research Grant Program Element 0601153N. Computational resources for the COAMPS-TC forecasts were provided by the Navy Department of Defense Supercomputing Resource Center in Stennis, Mississippi. We thank APL engineers Alex de Klerk, Phil Bush, and Brenton Salmi for their work to prepare and test the microSWIFTs. This material is based upon work supported by the National Science Foundation Graduate Research Fellowship Program under Grant (NSF Grant DGE-2140004). Any opinions, findings, and conclusions or recommendations expressed in this material are those of the author(s) and do not necessarily reflect the views of the National Science Foundation.

References

Amador, A., Merrifield, S. T., & Terrill, E. J. (2023). Assessment of atmospheric and oceanographic measurements from an autonomous surface vehicle. *Journal of Atmospheric and Oceanic Technology*, *40*(3), 305–326. https://doi.org/10.1175/JTECH-D-22-0060.1

Anctil, F., & Donelan, M. A. (1996). Air–water momentum flux observations over shoaling waves. *Journal of Physical Oceanography*, *26*(7), 1344–1353. https://doi.org/10.1175/1520-0485(1996)026⟨1344:AMFOOS⟩2.0.CO;2

Arakawa, H. (1954). On the pyramidal, mountainous, and confused sea in the right or dangerous semi-circle of typhoon. *Meteorology and Geophysics Papers*.

Banner, M. L. (1990). Equilibrium spectra of wind waves. *Journal of Physical Oceanography*, *20*(7), 966–984. https://doi.org/10.1175/1520-0485(1990)020⟨0966:ESOWW⟩2.0.CO;2

Banner, M. L., Gemmrich, J. R., & Farmer, D. M. (2002). Multiscale measurements of ocean wave breaking probability. *Journal of Physical Oceanography*, *32*(12), 3364–3375. https://doi.org/10.1175/1520-0485(2002)032⟨3364:MMOOWB⟩2.0.CO;2

Black, P. G., D'Asaro, E. A., Drennan, W. M., French, J. R., Niiler, P. P., Sanford, T. B., et al. (2007). Air–Sea exchange in hurricanes: Synthesis of observations from the coupled boundary layer Air–Sea transfer experiment. *Bulletin of the American Meteorological Society*, *88*(3), 357–374. https://doi.org/10.1175/BAMS-88-3-357

Boisot, O., Pioch, S., Fatras, C., Caulliez, G., Bringer, A., Borderies, P., et al. (2015). Ka-band backscattering from water surface at small incidence: A wind-wave tank study. *Journal of Geophysical Research: Oceans*, *120*(5), 3261–3285. https://doi.org/10.1002/2014JC010338

Bréon, F. M., & Henriot, N. (2006). Spaceborne observations of ocean glint reflectance and modeling of wave slope distributions. *Journal of Geophysical Research*, *111*(C6), C06005. https://doi.org/10.1029/2005JC003343

Buckley, M. P., & Veron, F. (2016). Structure of the airflow above surface waves. *Journal of Physical Oceanography*, *46*(5), 1377–1397. https://doi.org/10.1175/JPO-D-15-0135.1

Cangialosi, J. P., & Alaka, L. (2024). *Hurricane Idalia (AL102023) (national hurricane center tropical cyclone report)*. National Hurricane Center.

Charnock, H. (1955). Wind stress on a water surface. *Quarterly Journal of the Royal Meteorological Society*, *81*(350), 639–640. https://doi.org/10.1002/qj.49708135027

Chen, D. D., Ruf, C. S., & Gleason, S. T. (2016). Response time of mean square slope to wind forcing: An empirical investigation. *Journal of Geophysical Research: Oceans*, *121*(4), 2809–2823. https://doi.org/10.1002/2016JC011661

Chen, P., Zheng, G., Hauser, D., & Xu, F. (2018). Quasi-Gaussian probability density function of sea wave slopes from near nadir Ku-band radar observations. *Remote Sensing of Environment*, *217*, 86–100. https://doi.org/10.1016/j.rse.2018.07.027

Chen, S., Qiao, F., Zhang, J. A., Xue, Y., Ma, H., & Chen, S. (2022). Observed drag coefficient asymmetry in a tropical cyclone. *Journal of Geophysical Research: Oceans*, *127*(9), e2021JC018360. https://doi.org/10.1029/2021JC018360

Chen, X., Ginis, I., & Hara, T. (2020). Impact of shoaling ocean surface waves on wind stress and drag coefficient in coastal waters: 2. Tropical cyclones. *Journal of Geophysical Research: Oceans*, *125*(7). https://doi.org/10.1029/2020JC016223

Christie, D. C. (2024). Efficient estimation of directional wave buoy spectra using a reformulated Maximum Shannon Entropy Method: Analysis and comparisons for coastal wave datasets. *Applied Ocean Research*, *142*, 103830. https://doi.org/10.1016/j.apor.2023.103830

Clarizia, M. P., & Ruf, C. S. (2016). Wind speed retrieval algorithm for the cyclone global navigation satellite system (CYGNSS) mission. *IEEE Transactions on Geoscience and Remote Sensing*, *54*(8), 4419–4432. https://doi.org/10.1109/TGRS.2016.2541343

Collins, C. O., Blomquist, B., Persson, O., Lund, B., Rogers, W. E., Thomson, J., et al. (2017). Doppler correction of wave frequency spectra measured by underway vessels. *Journal of Atmospheric and Oceanic Technology*, *34*(2), 429–436. https://doi.org/10.1175/JTECH-D-16-0138.1

Collins, C. O., Potter, H., Lund, B., Tamura, H., & Graber, H. C. (2018). Directional wave spectra observed during intense tropical cyclones. *Journal of Geophysical Research: Oceans*, *123*(2), 773–793. https://doi.org/10.1002/2017JC012943

Colosi, L., Pizzo, N., Grare, L., Statom, N., & Lenain, L. (2023). Observations of surface gravity wave spectra from moving platforms. *Journal of Atmospheric and Oceanic Technology*, *40*(10), 1153–1169. https://doi.org/10.1175/JTECH-D-23-0022.1

Cox, C., & Munk, W. (1954). Measurement of the roughness of the sea surface from photographs of the sun's glitter. *Journal of the Optical Society of America*, *44*(11), 838. https://doi.org/10.1364/JOSA.44.000838

Curcic, M., & Haus, B. K. (2020). Revised estimates of ocean surface drag in strong winds. *Geophysical Research Letters*, *47*(10), e2020GL087647. https://doi.org/10.1029/2020GL087647

Davis, C., Wang, W., Chen, S. S., Chen, Y., Corbosiero, K., DeMaria, M., et al. (2008). Prediction of landfalling hurricanes with the advanced hurricane WRF model. *Monthly Weather Review*, *136*(6), 1990–2005. https://doi.org/10.1175/2007MWR2085.1

Davis, J., Thomson, J., Butterworth, B. J., Houghton, I. A., Fairall, C., Thompson, E. J., & De Boer, G. (2024). Multiscale measurements of hurricane waves using buoys and airborne radar. In *2024 IEEE/OES thirteenth current, waves and turbulence measurement (CWTM)* (pp. 1–8). IEEE. https://doi.org/10.1109/CWTM61020.2024.10526332

Davis, J., Thomson, J., Houghton, I. A., Doyle, J. D., Komaromi, W. A., Fairall, C. W., et al. (2023). Saturation of ocean surface wave slopes observed during hurricanes. *Geophysical Research Letters*, *50*(16). https://doi.org/10.1029/2023GL104139

Davis, J. R. (2024). Code for: Ocean surface wave slopes and wind-wave alignment observed in Hurricane Idalia. *Zenodo*. [Software]. https://doi.org/10.5281/zenodo.13953570

Davis, J. R., Thomson, J., Houghton, I. A., Fairall, C. W., Butterworth, B. J., Thompson, E. J., et al. (2024). Data for: Ocean surface wave slopes and wind-wave alignment observed in Hurricane Idalia. *Dryad*. [Dataset]. https://doi.org/10.5061/dryad.zw3r228h7

Donelan, M. A. (2018). On the decrease of the oceanic drag coefficient in high winds. *Journal of Geophysical Research: Oceans*, *123*(2), 1485–1501. https://doi.org/10.1002/2017JC013394

Donelan, M. A., Curcic, M., Chen, S. S., & Magnusson, A. K. (2012). Modeling waves and wind stress. *Journal of Geophysical Research*, *117*(C11). https://doi.org/10.1029/2011JC007787

Donelan, M. A., Haus, B. K., Reul, N., Plant, W. J., Stiassnie, M., Graber, H. C., et al. (2004). On the limiting aerodynamic roughness of the ocean in very strong winds. *Geophysical Research Letters*, *31*(18). https://doi.org/10.1029/2004GL019460

Dorsay, C., Egan, G., Houghton, I., Hegermiller, C., & Smit, P. B. (2023). Proxy observations of surface wind from a globally distributed network of wave buoys. *Journal of Atmospheric and Oceanic Technology*, *40*(12), 1591–1603. https://doi.org/10.1175/JTECH-D-23-0044.1

Dorsay, C., Houghton, I., Davis, J., Thomson, J., Smit, P., & Stackpole, E. (2023). Aerial deployment of spotter wave buoys during hurricane ian. In *Oceans 2023 - MTS/IEEE U.S. Gulf coast* (pp. 1–5). : IEEE. https://doi.org/10.23919/OCEANS52994.2023.10337056

Doyle, J., Hodur, R., Chen, S., Jin, Y., Msokaitis, J., Wang, S., et al. (2014). Tropical cyclone prediction using COAMPS-TC. *Oceanography*, *27*(3), 104–115. https://doi.org/10.5670/oceanog.2014.72

Doyle, J., Jin, Y., Hodur, R. M., Chen, S., Jin, H., Moskaitis, J., et al. (2012). *Real-time tropical cyclone prediction using COAMPS-TC*. In (pp. 15–28). https://doi.org/10.1142/9789814405683_0002

Doyle, J. D. (2002). Coupled atmosphere–ocean wave Simulations under high wind conditions. *Monthly Weather Review*, *130*(12), 3087–3099. https://doi.org/10.1175/1520-0493(2002)130⟨3087:CAOWSU⟩2.0.CO;2

Drennan, W. M., Graber, H. C., Hauser, D., & Quentin, C. (2003). On the wave age dependence of wind stress over pure wind seas. *Journal of Geophysical Research*, *108*(C3), 8062. https://doi.org/10.1029/2000JC000715

Edson, J. B., Jampana, V., Weller, R. A., Bigorre, S. P., Plueddemann, A. J., Fairall, C. W., et al. (2013). On the exchange of momentum over the open ocean. *Journal of Physical Oceanography*, *43*(8), 1589–1610. https://doi.org/10.1175/JPO-D-12-0173.1

Elfouhaily, T., Chapron, B., Katsaros, K., & Vandemark, D. (1997). A unified directional spectrum for long and short wind-driven waves. *Journal of Geophysical Research*, *102*(C7), 15781–15796. https://doi.org/10.1029/97JC00467

Emanuel, K. (2003). A similarity hypothesis for air–sea exchange at extreme wind speeds. *Journal of the Atmospheric Sciences*, *60*(11), 1420–1428. https://doi.org/10.1175/1520-0469(2003)060⟨1420:ASHFAE⟩2.0.CO;2

Forristall, G. Z. (1981). Measurements of a saturated range in ocean wave spectra. *Journal of Geophysical Research*, *86*(C9), 8075–8084. https://doi.org/10.1029/JC086iC09p08075

Gahtan, J., Knapp, K. R., Schreck, C. J. I., Diamond, H. J., Kossin, J. P., & Kruk, M. C. (2024). *International best track archive for climate stewardship (IBTrACS) project v4.01 (last 3 years)*. NOAA National Centers for Environmental Information. https://doi.org/10.25921/82ty-9e16

GEBCO Bathymetric Compilation Group. (2023). *The GEBCO_2023 Grid - a continuous terrain model of the global oceans and land*. NERC EDS British Oceanographic Data Centre NOC. https://doi.org/10.5285/f98b053b-0cbc-6c23-e053-6c86abc0af7b

Gleason, S., Zavorotny, V. U., Akos, D. M., Hrbek, S., PopStefanija, I., Walsh, E. J., et al. (2018). Study of surface wind and mean square slope correlation in hurricane ike with multiple sensors. *Ieee Journal of Selected Topics in Applied Earth Observations and Remote Sensing*, *11*(6), 1975–1988. https://doi.org/10.1109/JSTARS.2018.2827045

Guérin, C.-A., Capelle, V., & Hartmann, J.-M. (2022). Revisiting the Cox and Munk wave-slope statistics using IASI observations of the sea surface. *Remote Sensing of Environment*.

Hauser, D., Caudal, G., Guimbard, S., & Mouche, A. A. (2008). A study of the slope probability density function of the ocean waves from radar observations. *Journal of Geophysical Research*, *113*(C2), 2007JC004264. https://doi.org/10.1029/2007JC004264

Hauser, D., Tison, C., Amiot, T., Delaye, L., Corcoral, N., & Castillan, P. (2017). Swim: The first spaceborne wave scatterometer. *IEEE Transactions on Geoscience and Remote Sensing*, *55*(5), 3000–3014. https://doi.org/10.1109/TGRS.2017.2658672

Herbers, T. H. C., Jessen, P. F., Janssen, T. T., Colbert, D. B., & MacMahan, J. H. (2012). Observing Ocean surface waves with GPS-tracked buoys. *Journal of Atmospheric and Oceanic Technology*, *29*(7), 944–959. https://doi.org/10.1175/JTECH-D-11-00128.1

Holthuijsen, L. H. (2007). *Waves in oceanic and coastal waters*. Cambridge University Press. https://doi.org/10.1017/CBO9780511618536

Holthuijsen, L. H., Powell, M. D., & Pietrzak, J. D. (2012). Wind and waves in extreme hurricanes. *Journal of Geophysical Research*, *117*(C9). https://doi.org/10.1029/2012JC007983

Houghton, I., Smit, P., Clark, D., Dunning, C., Fisher, A., Nidzieko, N., et al. (2021). Performance statistics of a real-time Pacific Ocean weather sensor network. *Journal of Atmospheric and Oceanic Technology*, *38*(5), 1047–1058. https://doi.org/10.1175/JTECH-D-20-0187.1

Hsu, J.-Y. (2021). Observing surface wave directional spectra under typhoon megi (2010) using subsurface EM-APEX floats. *Journal of Atmospheric and Oceanic Technology*, *38*(11), 1949–1966. https://doi.org/10.1175/JTECH-D-20-0210.1

Hu, K., & Chen, Q. (2011). Directional spectra of hurricane-generated waves in the Gulf of Mexico. *Geophysical Research Letters*, *38*(19). https://doi.org/10.1029/2011GL049145

Husain, N. T., Hara, T., & Sullivan, P. P. (2022). Wind turbulence over misaligned surface waves and air–sea momentum flux. Part II: Waves in oblique wind. *Journal of Physical Oceanography*, *52*(1), 141–159. https://doi.org/10.1175/JPO-D-21-0044.1

Hwang, P. A. (2005). Wave number spectrum and mean square slope of intermediate-scale ocean surface waves. *Journal of Geophysical Research*, *110*(C10). https://doi.org/10.1029/2005JC003002

Hwang, P. A., Ainsworth, T. L., & Ouellette, J. D. (2021). Microwave specular measurements and ocean surface wave properties. *Sensors*, *21*(4), 1486. https://doi.org/10.3390/s21041486

Hwang, P. A., & Fan, Y. (2018). Low-frequency mean square slopes and dominant wave spectral properties: Toward tropical cyclone remote sensing. *IEEE Transactions on Geoscience and Remote Sensing*, *56*(12), 7359–7368. https://doi.org/10.1109/TGRS.2018.2850969

Hwang, P. A., Fan, Y., Ocampo-Torres, F. J., & García-Nava, H. (2017). Ocean surface wave spectra inside tropical cyclones. *Journal of Physical Oceanography*, *47*(10), 2393–2417. https://doi.org/10.1175/JPO-D-17-0066.1

Hwang, P. A., & Shemdin, O. H. (1988). The dependence of sea surface slope on atmospheric stability and swell conditions. *Journal of Geophysical Research*, *93*(C11), 13903–13912. https://doi.org/10.1029/jc093ic11p13903

Iyer, S., Thomson, J., Thompson, E., & Drushka, K. (2022). Variations in wave slope and momentum flux from wave-current interactions in the tropical trade winds. *Journal of Geophysical Research: Oceans*, *127*(3). https://doi.org/10.1029/2021JC018003

Jackson, F. C., Walton, W. T., Hines, D. E., Walter, B. A., & Peng, C. Y. (1992). Sea surface mean square slope from {\textit{{K}}}_{ \textrm {\textit{u} }} -band backscatter data. *Journal of Geophysical Research*, *97*(C7), 11411–11427. https://doi.org/10.1029/92JC00766

Janssen, P. A. E. M. (1989). Wave-induced stress and the drag of air flow over sea waves. *Journal of Physical Oceanography*, *19*(6), 745–754. (Place: Boston MA, USA Publisher: American Meteorological Society). https://doi.org/10.1175/1520-0485(1989)019⟨0745:WISATD⟩2.0.CO;2

Jiménez, P. A., & Dudhia, J. (2018). On the need to modify the sea surface roughness formulation over shallow waters. *Journal of Applied Meteorology and Climatology*, *57*(5), 1101–1110. https://doi.org/10.1175/JAMC-D-17-0137.1

Katzberg, S. J., Dunion, J., & Ganoe, G. G. (2013). The use of reflected GPS signals to retrieve ocean surface wind speeds in tropical cyclones. *Radio Science*, *48*(4), 371–387. https://doi.org/10.1002/rds.20042

King, D. B., & Shemdin, O. H. (1978). Radar observation of hurricane wave directions. In *Coastal engineering 1978* (pp. 209–226). American Society of Civil Engineers. https://doi.org/10.1061/9780872621909.012

Knapp, K. R., Kruk, M. C., Levinson, D. H., Diamond, H. J., & Neumann, C. J. (2010). The international best track archive for climate stewardship (IBTrACS): Unifying tropical cyclone data. *Bulletin of the American Meteorological Society*, *91*(3), 363–376. https://doi.org/10.1175/2009BAMS2755.1

Kobune, K., & Hashimoto, N. (1986). *Estimation of directional spectra from the maximum entropy principle*. In (pp. 80–85). Tokyo.

Kovesi, P. (2015). Good colour maps: How to design them. *arXiv*.

Kudryavtsev, V., Yurovskaya, M., & Chapron, B. (2021). Self-similarity of surface wave developments under tropical cyclones. *Journal of Geophysical Research: Oceans*, *126*(4), e2020JC016916. https://doi.org/10.1029/2020JC016916

Kuik, A. J., van Vledder, G. P., & Holthuijsen, L. H. (1988). A method for the routine analysis of pitch-and-roll buoy wave data. *Journal of Physical Oceanography*, *18*(7), 1020–1034. https://doi.org/10.1175/1520-0485(1988)018⟨1020:AMFTRA⟩2.0.CO;2

Lenain, L., & Melville, W. K. (2017). Measurements of the directional spectrum across the equilibrium saturation ranges of wind-generated surface waves. *Journal of Physical Oceanography*, *47*(8), 2123–2138. https://doi.org/10.1175/JPO-D-17-0017.1

Lenain, L., & Pizzo, N. (2020). The contribution of high-frequency wind-generated surface waves to the Stokes drift. *Journal of Physical Oceanography*, *50*(12), 3455–3465. https://doi.org/10.1175/JPO-D-20-0116.1

Lenain, L., Statom, N. M., & Melville, W. K. (2019). Airborne measurements of surface wind and slope statistics over the ocean. *Journal of Physical Oceanography*, *49*(11), 2799–2814. https://doi.org/10.1175/JPO-D-19-0098.1

Li, X., Karaev, V., Panfilova, M., Liu, B., Wang, Z., Xu, Y., et al. (2022). Measurements of total sea surface mean square slope field based on SWIM data. *IEEE Transactions on Geoscience and Remote Sensing*, *60*, 1–9. https://doi.org/10.1109/TGRS.2022.3174392

Longuet-Higgins, M. S. (1986). Eulerian and Lagrangian aspects of surface waves. *Journal of Fluid Mechanics*, *173*, 683–707. https://doi.org/10.1017/S0022112086001325

Manzella, E., Hara, T., & Sullivan, P. P. (2024). Reduction of drag coefficient due to misaligned wind-waves. *Journal of Geophysical Research: Oceans*, *129*(5), e2023JC020593. https://doi.org/10.1029/2023JC020593

Mudd, K. C., Ho, A., Amador, A., Lodise, J., Behrens, J., & Merrifield, S. T. (2024). Wind velocity estimates from wave observing platforms. *Coastal Engineering Journal*, *66*(3), 479–491. https://doi.org/10.1080/21664250.2024.2321660

NOAA National Data Buoy Center. (1971). Meteorological and oceanographic data collected from the national data buoy center coastal-marine automated network (C-MAN) and moored (weather) buoys. Station 42036 (LLNR 855) - west TAMPA [Dataset]. *NOAA National Centers for Environmental Information*. Retrieved from https://www.ncei.noaa.gov/archive/accession/NDBC-CMANWx

Phillips, O. M. (1985). Spectral and statistical properties of the equilibrium range in wind-generated gravity waves. *Journal of Fluid Mechanics*, *156*(-1), 505. https://doi.org/10.1017/S0022112085002221

Plant, W. J. (1982). A relationship between wind stress and wave slope. *Journal of Geophysical Research*, *87*(C3), 1961–1967. https://doi.org/10.1029/JC087iC03p01961

PopStefanija, I., Fairall, C. W., & Walsh, E. J. (2021). Mapping of directional ocean wave spectra in hurricanes and other environments. *IEEE Transactions on Geoscience and Remote Sensing*, *59*(11), 9007–9020. https://doi.org/10.1109/TGRS.2020.3042904

Potter, H., Collins, C. O., & Ortiz-Suslow, D. G. (2022). Pier-based measurements of air-sea momentum fluxes over shoaling waves during DUNEX. *Journal of Geophysical Research: Oceans*, *127*(11). https://doi.org/10.1029/2022JC018801

Powell, M. D., Vickery, P. J., & Reinhold, T. A. (2003). Reduced drag coefficient for high wind speeds in tropical cyclones. *Nature*, *422*(6929), 279–283. https://doi.org/10.1038/nature01481

Raghukumar, K., Chang, G., Spada, F., Jones, C., Janssen, T., & Gans, A. (2019). Performance characteristics of "spotter," a newly developed real-time wave measurement buoy. *Journal of Atmospheric and Oceanic Technology*, *36*(6), 1127–1141. https://doi.org/10.1175/JTECH-D-18-0151.1

Reichl, B. G., Hara, T., & Ginis, I. (2014). Sea state dependence of the wind stress over the ocean under hurricane winds. *Journal of Geophysical Research: Oceans*, *119*(1), 30–51. https://doi.org/10.1002/2013JC009289

Richter, D. H., Bohac, R., & Stern, D. P. (2016). An assessment of the flux profile method for determining air–sea momentum and enthalpy fluxes from dropsonde data in tropical cyclones. *Journal of the Atmospheric Sciences*, *73*(7), 2665–2682. https://doi.org/10.1175/JAS-D-15-0331.1

Richter, D. H., Wainwright, C., Stern, D. P., Bryan, G. H., & Chavas, D. (2021). Potential low bias in high-wind drag coefficient inferred from dropsonde data in hurricanes. *Journal of the Atmospheric Sciences*. https://doi.org/10.1175/JAS-D-20-0390.1

Romero, L., & Lubana, K. (2022). On the bimodality of the wind-wave spectrum: Mean-Squared-Slopes and azimuthal overlap integral. *Journal of Physical Oceanography*, *52*(7), 1549–1562. https://doi.org/10.1175/JPO-D-21-0299.1

Romero, L., Melville, W. K., & Kleiss, J. M. (2012). Spectral energy dissipation due to surface wave breaking. *Journal of Physical Oceanography*, *42*(9), 1421–1444. https://doi.org/10.1175/JPO-D-11-072.1

Ross, V., & Dion, D. (2007). Sea surface slope statistics derived from Sun glint radiance measurements and their apparent dependence on sensor elevation. *Journal of Geophysical Research*, *112*(C9), C09015. https://doi.org/10.1029/2007JC004137

Samelson, R. M. (2022). Wind drift in a homogeneous equilibrium sea. *Journal of Physical Oceanography*, *52*(9), 1945–1967. https://doi.org/10.1175/JPO-D-22-0017.1

Sauvage, C., Seo, H., Barr, B. W., Edson, J. B., & Clayson, C. A. (2024). Misaligned wind-waves behind atmospheric cold fronts. *Journal of Geophysical Research: Oceans*, *129*(9), e2024JC021162. https://doi.org/10.1029/2024JC021162

Schönau, M. C., Paluszkiewicz, T., Centurioni, L. R., Komaromi, W. A., Jin, H., & Doyle, J. D. (2024). In situ observations at the air-sea interface by expendable air-deployed drifters under hurricane Michael (2018). *Geophysical Research Letters*, *51*(5), e2023GL105730. https://doi.org/10.1029/2023GL105730

Schwendeman, M., Thomson, J., & Gemmrich, J. R. (2014). Wave breaking dissipation in a Young wind sea. *Journal of Physical Oceanography*, *44*(1), 104–127. https://doi.org/10.1175/JPO-D-12-0237.1

Shaw, J. A., & Churnside, J. H. (1997). Scanning-laser glint measurements of sea-surface slope statistics. *Applied Optics*, *36*(18), 4202–4213. https://doi.org/10.1364/AO.36.004202

Shimura, T., Mori, N., Baba, Y., & Miyashita, T. (2022). Ocean surface wind estimation from waves based on small GPS buoy observations in a bay and the open Ocean. *Journal of Geophysical Research: Oceans*, *127*(9), e2022JC018786. https://doi.org/10.1029/2022JC018786

Shimura, T., Mori, N., & Miyashita, T. (2024). Footprint of the air-sea momentum transfer saturation observed by ocean wave buoy network in extreme tropical cyclones. *Coastal Engineering*, *191*, 104537. https://doi.org/10.1016/j.coastaleng.2024.104537

Sullivan, P. P., Banner, M. L., Morison, R. P., & Peirson, W. L. (2018). Turbulent flow over steep steady and unsteady waves under strong wind forcing. *Journal of Physical Oceanography*, *48*(1), 3–27. https://doi.org/10.1175/JPO-D-17-0118.1

Sun, J., Vandemark, D., Mahrt, L., Vickers, D., Crawford, T., & Vogel, C. (2001). Momentum transfer over the coastal zone. *Journal of Geophysical Research*, *106*(D12), 12437–12448. https://doi.org/10.1029/2000JD900696

Takagaki, N., Komori, S., Suzuki, N., Iwano, K., Kuramoto, T., Shimada, S., et al. (2012). Strong correlation between the drag coefficient and the shape of the wind sea spectrum over a broad range of wind speeds. *Geophysical Research Letters*, *39*(23). https://doi.org/10.1029/2012GL053988

Tamizi, A., & Young, I. R. (2020). The spatial distribution of ocean waves in tropical cyclones. *Journal of Physical Oceanography*, *50*(8), 2123–2139. https://doi.org/10.1175/JPO-D-20-0020.1

Tannehill, I. R. (1936). Sea swells in relation to movement and intensity of tropical storms. *Monthly Weather Review*, *64*(7), 231–238. https://doi.org/10.1175/1520-0493(1936)64⟨231b:SSIRTM⟩2.0.CO;2

Taylor, P. K., & Yelland, M. J. (2001). The dependence of sea surface roughness on the height and steepness of the waves. *Journal of Physical Oceanography*, *31*(2), 572–590. https://doi.org/10.1175/1520-0485(2001)031⟨0572:TDOSSR⟩2.0.CO;2

Thomson, J., Bush, P., Castillo Contreras, V., Clemett, N., Davis, J., De Klerk, A., et al. (2023). Development and testing of microSWIFT expendable wave buoys. *Coastal Engineering Journal*, *66*, 1–13. https://doi.org/10.1080/21664250.2023.2283325

Thomson, J., D'Asaro, E. A., Cronin, M. F., Rogers, W. E., Harcourt, R. R., & Shcherbina, A. (2013). Waves and the equilibrium range at ocean weather station P. *Journal of Geophysical Research: Oceans*, *118*(11), 5951–5962. https://doi.org/10.1002/2013JC008837

Thomson, J., Girton, J. B., Jha, R., & Trapani, A. (2018). Measurements of directional wave spectra and wind stress from a wave glider autonomous surface vehicle. *Journal of Atmospheric and Oceanic Technology*, *35*(2), 17–363. https://doi.org/10.1175/jtech-d-17-0091.1

Thyng, K., Greene, C., Hetland, R., Zimmerle, H., & DiMarco, S. (2016). True colors of oceanography: Guidelines for effective and accurate colormap selection. *Oceanography*, *29*(3), 9–13. https://doi.org/10.5670/oceanog.2016.66

Toba, Y. (1973). Local balance in the air-sea boundary processes. *Journal of the Oceanographical Society of Japan*, *29*(2), 209–220. https://doi.org/10.1007/bf02109506

Toba, Y., Iida, N., Kawamura, H., Ebuchi, N., & Jones, I. S. F. (1990). Wave dependence of sea-surface wind stress. *Journal of Physical Oceanography*, *20*(5), 705–721. https://doi.org/10.1175/1520-0485(1990)020⟨0705:WDOSSW⟩2.0.CO;2

Vandemark, D., Chapron, B., Sun, J., Crescenti, G. H., & Graber, H. C. (2004). Ocean wave slope observations using radar backscatter and laser altimeters. *Journal of Physical Oceanography*, *34*(12), 2825–2842. https://doi.org/10.1175/JPO2663.1

Vincent, C. L., Thomson, J., Graber, H. C., & Collins, C. O. (2019). Impact of swell on the wind-sea and resulting modulation of stress. *Progress in Oceanography*, *178*, 102164. https://doi.org/10.1016/j.pocean.2019.102164

Voermans, J. J., Smit, P. B., Janssen, T. T., & Babanin, A. V. (2020). Estimating wind speed and direction using wave spectra. *Journal of Geophysical Research: Oceans*, *125*(2). https://doi.org/10.1029/2019JC015717

Walsh, E. J., PopStefanija, I., Matrosov, S. Y., Zhang, J., Uhlhorn, E., & Klotz, B. (2014). Airborne rain-rate measurement with a wide-swath radar altimeter. *Journal of Atmospheric and Oceanic Technology*, *31*(4), 860–875. https://doi.org/10.1175/JTECH-D-13-00111.1

Walsh, E. J., Vandemark, D. C., Friehe, C. A., Burns, S. P., Khelif, D., Swift, R. N., & Scott, J. F. (1998). Measuring sea surface mean square slope with a 36-GHz scanning radar altimeter. *Journal of Geophysical Research*, *103*(C6), 12587–12601. https://doi.org/10.1029/97JC02443

Wright, C. W., Walsh, E. J., Vandemark, D., Krabill, W. B., Garcia, A. W., Houston, S. H., et al. (2001). Hurricane directional wave spectrum spatial variation in the open ocean. *Journal of Physical Oceanography*, *31*(8), 2472–2488. https://doi.org/10.1175/1520-0485(2001)031⟨2472:HDWSSV⟩2.0.CO;2

Wright, E. E., Bourassa, M. A., Stoffelen, A., & Bidlot, J.-R. (2021). Characterizing buoy wind speed error in high winds and varying sea state with ASCAT and ERA5. *Remote Sensing*, *13*(22), 4558. https://doi.org/10.3390/rs13224558

Wu, J. (1990). Mean square slopes of the wind-disturbed water surface, their magnitude, directionality, and composition. *Radio Science*, *25*(1), 37–48. https://doi.org/10.1029/RS025i001p00037

Young, I. R. (2003). A review of the sea state generated by hurricanes. *Marine Structures*, *16*(3), 201–218. https://doi.org/10.1016/S0951-8339(02)00054-0

Young, I. R. (2006). Directional spectra of hurricane wind waves. *Journal of Geophysical Research*, *111*(C8). https://doi.org/10.1029/2006JC003540

Zappa, C. J., Banner, M. L., Schultz, H., Corrada-Emmanuel, A., Wolff, L. B., & Yalcin, J. (2008). Retrieval of short ocean wave slope using polarimetric imaging. *Measurement Science and Technology*, *19*(5), 055503. https://doi.org/10.1088/0957-0233/19/5/055503

Zhong, Y.-Z., Chien, H., Chang, H.-M., & Cheng, H.-Y. (2022). Ocean wind observation based on the mean square slope using a self-developed miniature wave buoy. *Sensors*, *22*(19), 7210. https://doi.org/10.3390/s22197210

Zhou, X., Hara, T., Ginis, I., D'Asaro, E., Hsu, J.-Y., & Reichl, B. G. (2022). Drag coefficient and its sea state dependence under tropical cyclones. *Journal of Physical Oceanography*, *52*(7), 1447–1470. https://doi.org/10.1175/JPO-D-21-0246.1

Zippel, S., & Thomson, J. (2017). Surface wave breaking over sheared currents: Observations from the mouth of the Columbia river. *Journal of Geophysical Research: Oceans*, *122*(4), 3311–3328. https://doi.org/10.1002/2016JC012498